

Dispersion controlled by permeable surfaces: surface properties and scaling

Bowen Ling^{1,2}, Alexandre M. Tartakovsky³ and Ilenia Battiato^{2,†}

¹Mechanical and Aerospace Engineering Department, University of California San Diego,
La Jolla, CA 92093, USA

²Mechanical Engineering Department, San Diego State University, San Diego, CA 92182, USA

³Fundamental and Computational Sciences Directorate, Pacific Northwest National Laboratory,
Richland, WA 99352, USA

(Received 20 November 2015; revised 16 May 2016; accepted 18 June 2016;
first published online 19 July 2016)

Permeable and porous surfaces are common in natural and engineered systems. Flow and transport above such surfaces are significantly affected by the surface properties, e.g. matrix porosity and permeability. However, the relationship between such properties and macroscopic solute transport is largely unknown. In this work, we focus on mass transport in a two-dimensional channel with permeable porous walls under fully developed laminar flow conditions. By means of perturbation theory and asymptotic analysis, we derive the set of upscaled equations describing mass transport in the coupled channel–porous-matrix system and an analytical expression relating the dispersion coefficient with the properties of the surface, namely porosity and permeability. Our analysis shows that their impact on the dispersion coefficient strongly depends on the magnitude of the Péclet number, i.e. on the interplay between diffusive and advective mass transport. Additionally, we demonstrate different scaling behaviours of the dispersion coefficient for thin or thick porous matrices. Our analysis shows the possibility of controlling the dispersion coefficient, i.e. transverse mixing, by either active (i.e. changing the operating conditions) or passive mechanisms (i.e. controlling matrix effective properties) for a given Péclet number. By elucidating the impact of matrix porosity and permeability on solute transport, our upscaled model lays the foundation for the improved understanding, control and design of microporous coatings with targeted macroscopic transport features.

Key words: low-Reynolds-number flows, micro-/nano-fluid dynamics, porous media

1. Introduction

The unique features of patterned surfaces and porous coatings have long been recognized (e.g. Marmur 2004). Of particular interest are coupled flows and transport processes through and above permeable and/or (micro-) patterned layers, as they are ubiquitous in environmental, biological and engineered systems. Examples of natural

† Email address for correspondence: ibattiato@mail.sdsu.edu

systems include transport in fractured rocks and flows over sediment beds (Nikora *et al.* 2001; Goharzadeh, Khalili & Jørgensen 2005; Battiato & Vollmer 2012; Liu *et al.* 2013), coral reefs and canopies (Nepf *et al.* 2007; Ghisalberti 2009; Papke & Battiato 2013; Battiato & Rubol 2014), nutrient uptake from roots (Marschner & Dell 1994; Gilroy & Jones 2000) and passive predatory strategies in some carnivorous plants (Lloyd *et al.* 1942; Goharzadeh *et al.* 2005; Scholz *et al.* 2010). Coupled flows are critical to many engineering applications including superhydrophobic (Ou, Perot & Rothstein 2004; Rothstein 2010; Battiato 2014) and slippery liquid-infused porous surfaces (Cui *et al.* 2015; Hou *et al.* 2015), shear sensors, flows in blood vessels (Weinbaum *et al.* 2003; Al-Chidiac *et al.* 2009) and above carbon nanotube forests (Deck *et al.* 2009; Battiato, Bandaru & Tartakovsky 2010; Battiato 2012), just to mention a few. Distinctive characteristics of microstructured surfaces and nanoimprints are routinely adopted in a variety of other manufacturing processes including, but not limited to, ultrafiltration of colloids (Maruf *et al.* 2013*b*) and nutrient delivery in bioreactor devices (Griffiths, Howell & Shipley 2013; Gruenberger *et al.* 2013). Channel transverse mixing is critical to, e.g., reduce membrane fouling or increase the overall reactivity of a system. This is particularly challenging in microfluidic devices where mixing is controlled by diffusion, with resulting slow reaction rates. Surface patterns have been successfully employed to enhance transverse mixing in microchannels (Stroock *et al.* 2002; Stroock & Whitesides 2003) and reduce membrane fouling (Weinman & Husson 2016). Yet, a clear connection between the properties of the surface and its macroscopic response still remains an open question (Bouquet & Lauga 2011). Notwithstanding significant theoretical advancements, attempts to relate surface properties to macroscopic quantities, such as the dispersion coefficient and average velocity, remain mostly phenomenological (e.g. Li, Reinhoudt & Crego-Calama 2007; Ybert *et al.* 2007; Maruf *et al.* 2013*a*; Hou *et al.* 2015), and analytical expressions are available only for tractable geometries (e.g. Lauga & Stone 2003; Davis & Lauga 2010).

Here, we consider non-reactive tracer transport through a symmetric (micro-)channel embedded in a permeable porous matrix, and characterize the latter by its permeability and porosity. In this work, we are concerned with analytically relating the macroscopic response of the coupled channel–matrix system, i.e. the longitudinal dispersion coefficient, with the porous layer porosity and permeability and the channel transport regimes. We assume that the flow and transport are governed by the combination of Stokes, Brinkman and advection–diffusion equations subject to appropriate initial and boundary conditions. This formulation, relevant for the study and control of transverse mixing in microchannels, is especially suitable for the modelling of Navier–Stokes flows (both laminar and turbulent) above patterned surfaces, e.g. micro-riblets (Battiato 2014) and carbon nanotube forests (Battiato *et al.* 2010; Battiato 2012), where the idealization of the pattern as a porous layer has been shown to be appropriate.

Two approaches are routinely employed to relate channel and matrix properties to dispersion in a coupled channel–matrix system: (i) analytical and semianalytical solutions of a system of coupled advection–diffusion equations (ADEs) and (ii) upscaling perturbative methods. While exact, analytical solutions of a system of ADEs can often be obtained only under restrictive simplifying assumptions. The greatest technical difficulty in (semi)analytically solving advection–diffusion equations is in accounting for the non-uniformity of the velocity profile in the channel and/or matrix. This complication is generally overcome, or better avoided, by assuming uniform velocity in the channel, purely diffusive transport in the matrix or both. The first analytical treatment of transport mechanisms in channel–matrix systems is generally

attributed to Tang, Frind & Sudicky (1981), who considered a one-dimensional thin channel embedded in an impermeable (to flow) porous matrix. Their result was later extended by Sudicky & Frind (1982) to account for the presence of neighbouring parallel channels. A detailed review of this approach is provided by Bodin, Delay & De Marsily (2003). More recently, Roubinet, Dreuzy & Tartakovsky (2012) solved semi-analytically the transport problem for a uniform flow in a two-dimensional channel embedded in an impermeable two-dimensional infinite matrix, where mass transport was purely diffusive.

Alternative approaches to connect macroscale transport properties to surface properties are upscaling methods, such as homogenization (Hornung 1997; Boso & Battiato 2013), volume averaging (Whitaker 1999), thermodynamically constrained averaging (Gray & Miller 2005), stochastic homogenization, the method of moments (Brenner 1987), etc. These approaches involve perturbative methods in various forms (single- and multiple-scale expansions, Reynolds-type decomposition, etc.), which allow rigorous derivation of the macroscale equations satisfied by spatially averaged microscale (pore-scale) quantities. The connection between the micro- and the macroscale is formally established through effective parameters (e.g. dispersion coefficient, effective contact angle, macroscopic reaction rates, slip velocity), which depend on the specific structure of the coupled channel–matrix system. Unlike (semi)analytical solutions, these methods allow one to relax many of the assumptions concerning the shape of the velocity profile in the channel–matrix system. This is achieved at the cost of obtaining an asymptotic approximation of the full microscopic solution, generally truncated at the first or second order. In this work, we focus on perturbative approaches, since our main objective is to explicitly account for steady non-uniform flow conditions and the impact of matrix permeability on dispersion.

Since the problem of transport in a channel (with or without porous walls) has been historically handled in the context of homogenization theory, we limit our attention to the results obtained with this specific technique. We emphasize that equivalent results have been achieved with other upscaling methods. The seminal result on the upscaling of passive tracer transport in a channel with planar walls is generally attributed to the works by Taylor (1953) and Aris (1956), who, by means of perturbation methods, derived the well-known Aris–Taylor formula for the dispersion coefficient. More recently, Mikelic, Devigne & Duijn (2006) studied transport in a two-dimensional channel with reactive walls. The leading-order solution was found by asymptotic homogenization and the two-dimensional solution obtained in terms of the leading-order solution and its first derivative. Recently, Dejam, Hassanzadeh & Chen (2014) coupled a two-dimensional ADE for the channel with a one-dimensional diffusion equation for the matrix. They considered a parabolic flow profile in the channel, and applied Reynolds decomposition to obtain an upscaled equation for the average concentration. By means of Laplace transform and numerical inverse Laplace transform, they studied transport dynamics for different Péclet numbers. Griffiths *et al.* (2013) considered transport in a cylindrical tube with a thin porous wall. In a two-domain approach, they coupled Stokes and Darcy flow by means of the Beavers and Joseph condition for the effective slip at the free-fluid–porous-medium interface (Beavers & Joseph 1967). Asymptotic analysis was used to derive the corresponding macroscopic equation and effective dispersion coefficient.

Here, we model a coupled system composed of a planar channel embedded in a porous matrix of prescribed porosity and permeability, and establish an analytical relationship between the effective transport properties of the system, i.e. macroscopic dispersion coefficient, those of the porous matrix, i.e. porosity and permeability, and

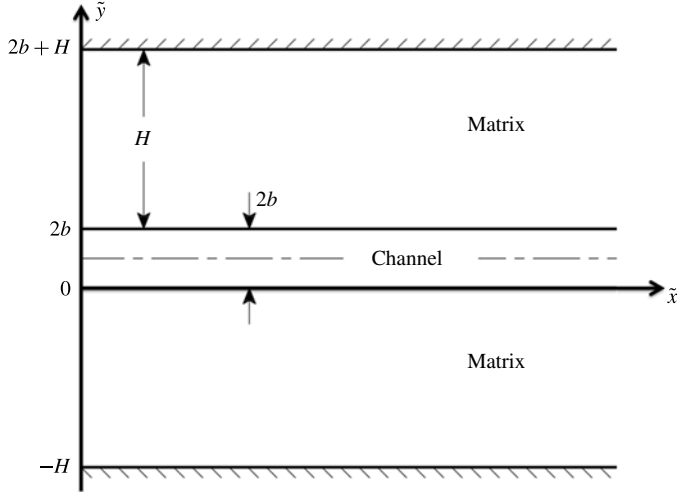


FIGURE 1. Problem domain.

different transport regimes identified by the Péclet number. We also investigate the scaling behaviour of the normalized dispersion in various limits and for thin and thick porous matrices.

The paper is organized as follows. In § 2 we provide the model formulation for flow and transport in a two-dimensional coupled channel–matrix system, in § 3 we present the upscaled (macroscopic) equations and in § 4 we provide an analytical relationship between the dispersion coefficient and the matrix properties. In § 4 we study the scaling behaviour of the dispersion coefficient and its threshold values in different limits. In § 5 we perform numerical simulations to test the upscaled model accuracy against two-dimensional simulations. Further, we perform a detailed comparison between the upscaled model derived here and that of Dejam *et al.* (2014), and highlight the range of applicability of each. Concluding remarks are given in § 6.

2. Model formulation

We consider tracer transport in a single-phase fully developed pressure-driven laminar flow in a semi-infinitely long (micro-)channel embedded in a porous matrix with permeability k and porosity ϕ (figure 1). While the Carman–Kozeny equation establishes a unique relationship between porosity and permeability, it is unable to describe permeability dependences over a broad range of porous medium configurations (Valdes-Parada, Ochoa-Tapia & Alvarez-Ramirez 2009). Without loss of generality, we consider porosity and permeability as independent variables in order to account for the unknown relationship between k and the microstructure arrangement. The boundaries between the channel and the matrix walls are located at $\tilde{y} = 0$ and $\tilde{y} = 2b$. The porous matrix width (thickness) is H , i.e. the matrix occupies the domains $\tilde{y} \in (2b, 2b + H)$ and $\tilde{y} \in (-H, 0)$. A dilute Newtonian solution with density ρ and solute concentration c_0 is injected at the domain inlet $\tilde{x} = 0$. Flow and transport occur both in the channel and in the matrix, and are affected by the momentum and mass transfer across the channel–matrix interfaces.

We denote the concentration and the \tilde{x} -component of the velocity in the channel and the matrix by \tilde{c}_f , \tilde{u}_f , \tilde{c}_m and \tilde{u}_m respectively. Due to the symmetry of the domain, we restrict our analysis to $\tilde{y} \in (-H, b)$.

2.1. Flow equations

Fully developed Stokes flow in the channel–matrix system can be described by coupling the Stokes equation in the channel with a Darcy–Brinkman equation in the matrix,

$$\mu \frac{d^2 \tilde{u}_f}{d\tilde{y}^2} - \frac{d\tilde{p}}{d\tilde{x}} = 0, \quad \tilde{y} \in (0, b), \quad (2.1a)$$

$$\mu \frac{d^2 \tilde{u}_m}{d\tilde{y}^2} - \frac{\mu}{k} \tilde{u}_m - \frac{d\tilde{p}}{d\tilde{x}} = 0, \quad \tilde{y} \in (-H, 0), \quad (2.1b)$$

respectively, where $\tilde{u}_i(\tilde{y})$ with $i = \{f, m\}$ is the \tilde{x} -component of the velocity in the channel and the matrix, μ is the fluid dynamic viscosity, $k[L^2]$ is the matrix permeability, and $d\tilde{p}/d\tilde{x}$ is a constant pressure gradient driving the flow in the \tilde{x} -direction. Equations (2.1) are subject to no-slip and symmetry boundary conditions at the bottom solid wall ($\tilde{y} = -H$) and channel centreline ($\tilde{y} = b$) respectively, and continuity of velocity and shear stress conditions at the interface separating the channel and the porous matrix ($\tilde{y} = 0$),

$$\tilde{u}_m|_{\tilde{y}=-H} = 0, \quad \left. \frac{d\tilde{u}_f}{d\tilde{y}} \right|_{\tilde{y}=b} = 0, \quad \tilde{u}_f|_{\tilde{y}=0} = \tilde{u}_m|_{\tilde{y}=0}, \quad \left. \frac{d\tilde{u}_f}{d\tilde{y}} \right|_{\tilde{y}=0} = \left. \frac{d\tilde{u}_m}{d\tilde{y}} \right|_{\tilde{y}=0}. \quad (2.2a-d)$$

While many boundary conditions have been proposed to couple free and filtration flows, see Le Bars & Worster (2006) for a review, continuity of velocity and shear stress has been proven accurate in a number of applications, e.g. Battiato *et al.* (2010), Battiato (2012) and Battiato & Rubol (2014).

We define the following dimensionless quantities:

$$x = \frac{\tilde{x}}{L}, \quad y = \frac{\tilde{y}}{b}, \quad p = \frac{\tilde{p}}{p_0}, \quad u_i = \frac{\tilde{u}_i}{U}, \quad \text{with } i = \{f, m\}, \quad (2.3a-d)$$

where L is a characteristic macroscopic/observation length scale, e.g. the distance far from the inlet where data are collected, p_0 is a characteristic pressure, e.g. the ambient pressure, and U is the average velocity across the channel. Then, (2.1)–(2.2) can be cast in dimensionless form,

$$\frac{d^2 u_f}{dy^2} - \Psi = 0, \quad y \in (0, 1), \quad (2.4a)$$

$$\frac{d^2 u_m}{dy^2} - \lambda^2 u_m - \Psi = 0, \quad y \in (-h, 0), \quad (2.4b)$$

subject to

$$u_m|_{y=-h} = 0, \quad \left. \frac{du_f}{dy} \right|_{y=1} = 0, \quad u_f|_{y=0} = u_m|_{y=0}, \quad \left. \frac{du_f}{dy} \right|_{y=0} = \left. \frac{du_m}{dy} \right|_{y=0}, \quad (2.5a-d)$$

where

$$\lambda^2 = \frac{b^2}{k}, \quad \Psi = \frac{p_0 b^2}{\mu UL} \frac{dp}{dx} \quad \text{and} \quad h = \frac{H}{b}. \quad (2.6a-c)$$

The system (2.4) admits an analytical solution for the velocity profiles in the channel and the matrix, u_f and u_m respectively,

$$u_f(y) = \frac{\Psi}{2}y^2 + Ay + B, \quad y \in [0, 1], \quad (2.7)$$

$$u_m(y) = -\frac{\Psi}{\lambda^2} + Ee^{\lambda y} + Fe^{-\lambda y}, \quad y \in [-h, 0], \quad (2.8)$$

where A , B , E and F are integration constants,

$$A = -\Psi, \quad (2.9a)$$

$$B = -\frac{\Psi}{\lambda^2}(-1 + e^\Lambda)(-1 + e^\Lambda + \lambda + \lambda e^\Lambda)(1 + e^{2\Lambda})^{-1}, \quad (2.9b)$$

$$E = -\frac{\Psi}{\lambda^2}e^\Lambda(-1 + \lambda e^\Lambda)(1 + e^{2\Lambda})^{-1}, \quad (2.9c)$$

$$F = -\frac{\Psi}{\lambda^2}(\lambda + e^\Lambda)(1 + e^{2\Lambda})^{-1}. \quad (2.9d)$$

Moreover,

$$\Lambda = \lambda h, \quad (2.10)$$

which represents a characteristic dimensionless length scale, also known as the penetration length, associated with the thickness of the boundary layer between the free and filtration flows (Nepf 2012). A classification between thin ($\Lambda \ll 1$) and thick porous media ($\Lambda \gg 1$) can be introduced based on the magnitude of Λ (Battiato 2012). The slip velocity, U_{slip} , can be readily calculated as $U_{slip} := u_m(y=0) = u_f(y=0)$, i.e.

$$U_{slip} = -\Psi \frac{h(e^\Lambda - 1)[\Lambda(e^\Lambda + 1) + h(e^\Lambda - 1)]}{\Lambda^2(1 + e^{2\Lambda})}. \quad (2.11)$$

2.2. Transport equations

We consider transport of a passive scalar injected at the channel inlet, i.e. $\tilde{x} = 0$ and $\tilde{y} \in (0, b)$, with concentration c_0 for $\tilde{t} > 0$. The solute concentrations in the channel \tilde{c}_f and the matrix \tilde{c}_m satisfy a system of coupled advection–dispersion equations,

$$\frac{\partial \tilde{c}_f}{\partial \tilde{t}} + \tilde{u}_f \frac{\partial \tilde{c}_f}{\partial \tilde{x}} = \tilde{D}_f \left(\frac{\partial^2 \tilde{c}_f}{\partial \tilde{x}^2} + \frac{\partial^2 \tilde{c}_f}{\partial \tilde{y}^2} \right), \quad \tilde{y} \in (0, b), \quad \tilde{x}, \tilde{t} > 0, \quad (2.12a)$$

$$\frac{\partial \tilde{c}_m}{\partial \tilde{t}} + \tilde{u}_m \frac{\partial \tilde{c}_m}{\partial \tilde{x}} = \tilde{D}_{mx} \frac{\partial^2 \tilde{c}_m}{\partial \tilde{x}^2} + \tilde{D}_{my} \frac{\partial^2 \tilde{c}_m}{\partial \tilde{y}^2}, \quad \tilde{y} \in (-H, 0), \quad \tilde{x}, \tilde{t} > 0, \quad (2.12b)$$

where \tilde{D}_f is the molecular diffusion coefficient, \tilde{D}_{mx} and \tilde{D}_{my} are the \tilde{x} and \tilde{y} components of the dispersion coefficient in the matrix, and $\tilde{u}_f = Uu_f$ and $\tilde{u}_m = Uu_m$ are defined by (2.7) and (2.8) respectively. Equations (2.12) are subject to initial,

$$\tilde{c}_f(\tilde{x}, \tilde{y}, \tilde{t} = 0) = 0 \quad \text{and} \quad \tilde{c}_m(\tilde{x}, \tilde{y}, \tilde{t} = 0) = 0, \quad (2.13a,b)$$

and boundary conditions,

$$\tilde{c}_f(0, \tilde{y} \in [0, b], \tilde{t}) = c_0, \quad \tilde{c}_f(\infty, \tilde{y} \in [0, b], \tilde{t}) = 0, \quad \frac{\partial \tilde{c}_f}{\partial \tilde{y}}(\tilde{x}, b, \tilde{t}) = 0, \quad (2.14a-c)$$

$$\frac{\partial \tilde{c}_m}{\partial \tilde{x}}(0, \tilde{y} \in [-H, 0], \tilde{t}) = 0, \quad \tilde{c}_m(\infty, \tilde{y} \in [-H, 0], \tilde{t}) = 0, \quad \frac{\partial \tilde{c}_m}{\partial \tilde{y}}(\tilde{x}, -H, \tilde{t}) = 0. \quad (2.15a-c)$$

Additionally, on the channel–matrix interface, the continuity of concentration and mass flux is satisfied,

$$\tilde{c}_f(\tilde{x}, 0, \tilde{t}) = \tilde{c}_m(\tilde{x}, 0, \tilde{t}) \quad \text{and} \quad \frac{\partial \tilde{c}_f}{\partial \tilde{y}}(\tilde{x}, 0, \tilde{t}) = \frac{\phi \tilde{D}_{my}}{\tilde{D}_f} \frac{\partial \tilde{c}_m}{\partial \tilde{y}}(\tilde{x}, 0, \tilde{t}), \quad (2.16a,b)$$

where ϕ is the matrix porosity. We define the following dimensionless quantities:

$$t = \frac{U}{L} \tilde{t}, \quad D_f = \frac{\tilde{D}_f}{D^*}, \quad D_{mi} = \frac{\tilde{D}_{mi}}{D^*}, \quad c_i = \frac{\tilde{c}_i}{c_0}, \quad \text{with } i = \{f, m\}. \quad (2.17a-d)$$

Here, $D^* = O(\tilde{D}_f)$ is the order of magnitude of the solute molecular diffusion coefficient, such that $D_f = O(1)$. Since we investigate the dynamics of transport in a time frame much larger than the diffusion time, $\tau_d = b^2/D^*$, and close to the advection time, $\tau_a = L/U$, all of the time scales are scaled by τ_a . Then, (2.12) can be written in dimensionless form as follows:

$$\epsilon Pe \frac{\partial c_f}{\partial t} + \epsilon Pe u_f \frac{\partial c_f}{\partial x} = \epsilon^2 D_f \frac{\partial^2 c_f}{\partial x^2} + D_f \frac{\partial^2 c_f}{\partial y^2}, \quad y \in (0, 1), \quad x, t > 0, \quad (2.18a)$$

$$\epsilon Pe \frac{\partial c_m}{\partial t} + \epsilon Pe u_m \frac{\partial c_m}{\partial x} = \epsilon^2 D_{mx} \frac{\partial^2 c_m}{\partial x^2} + D_{my} \frac{\partial^2 c_m}{\partial y^2}, \quad y \in (-h, 0), \quad x, t > 0, \quad (2.18b)$$

where

$$\epsilon = \frac{b}{L} \quad \text{and} \quad Pe = \frac{\tau_d}{\tau_a} = \frac{Ub}{D^*}. \quad (2.19a,b)$$

Equations (2.18) are subject to

$$c_f(0, y \in [0, 1], t) = 1, \quad c_f(\infty, y \in [0, 1], t) = 0, \quad \frac{\partial c_f}{\partial y}(x, 1, t) = 0, \quad (2.20a-c)$$

$$\frac{\partial c_m}{\partial x}(0, y \in [-h, 0], t) = 0, \quad c_m(\infty, y \in [-h, 0], t) = 0, \quad \frac{\partial c_m}{\partial y}(x, -h, t) = 0, \quad (2.21a-c)$$

$$c_f(x, 0, t) = c_m(x, 0, t) \quad \text{and} \quad \frac{\partial c_f}{\partial y}(x, 0, t) = \frac{\phi D_{my}}{D_f} \frac{\partial c_m}{\partial y}(x, 0, t). \quad (2.22a,b)$$

In the following section, we employ asymptotic homogenization to relate the dispersion coefficient in the coupled channel–matrix system with the effective properties of the matrix.

3. Asymptotic homogenization and upscaled equations

To derive the upscaled transport equations, we apply rescaling and asymptotic analysis to the ADEs (2.18). We introduce the rescaled longitudinal coordinate ξ and a coefficient α such that

$$x := \xi \sqrt{\epsilon} \quad \text{and} \quad Pe := \epsilon^{-\alpha}. \quad (3.1a,b)$$

Equations (2.18a) and (2.18b) take the form

$$\epsilon Pe \left(\frac{\partial c_f}{\partial t} + \frac{u_f}{\sqrt{\epsilon}} \frac{\partial c_f}{\partial \xi} \right) = \epsilon D_f \frac{\partial^2 c_f}{\partial \xi^2} + D_f \frac{\partial^2 c_f}{\partial y^2}, \quad (3.2a)$$

$$\epsilon Pe \left(\frac{\partial c_m}{\partial t} + \frac{u_m}{\sqrt{\epsilon}} \frac{\partial c_m}{\partial \xi} \right) = \epsilon D_{mx} \frac{\partial^2 c_m}{\partial \xi^2} + D_{my} \frac{\partial^2 c_m}{\partial y^2}. \quad (3.2b)$$

Let us define the cross-sectional averaging operator

$$\langle \cdot \rangle = \frac{1}{L^*} \int_0^{L^*} dy, \quad (3.3)$$

where $L^* = 1$ for the channel and $L^* = -h$ for the matrix. Moreover, we employ the *ansatz*

$$c_i = c_i^{(0)}(\xi, t) + \sqrt{\epsilon} c_i^{(1)}(\xi, y, t) + \epsilon c_i^{(2)}(\xi, y, t) + O(\epsilon\sqrt{\epsilon}), \quad i = \{f, m\}, \quad (3.4)$$

where $c_i^{(j)}$ is the j th-order term in the expansion of concentration c_i . Substituting (3.4) in (3.2) while applying the averaging operator (3.3) leads to a system of coupled upscaled (effective macroscopic) equations (see [Appendix](#))

$$\epsilon^2 Pe \left(\frac{\partial \langle c_f \rangle}{\partial t} + \langle u_f \rangle \frac{\partial \langle c_f \rangle}{\partial x} \right) = \epsilon^3 D_f^* \frac{\partial^2 \langle c_f \rangle}{\partial x^2} - \phi \left[\epsilon^2 Pe N_1 \frac{\partial \langle c_m \rangle}{\partial x} + \frac{3D_{my}}{h} (\langle c_f \rangle - \langle c_m \rangle) \right], \quad (3.5a)$$

$$\epsilon^2 Pe \left(\frac{\partial \langle c_m \rangle}{\partial t} + \langle u_m \rangle \frac{\partial \langle c_m \rangle}{\partial x} \right) = \epsilon^3 D_m^* \frac{\partial^2 \langle c_m \rangle}{\partial x^2} + \frac{1}{\phi} \left[\epsilon^2 Pe \frac{M_1}{h} \frac{\partial \langle c_f \rangle}{\partial x} + \frac{3D_f}{h} (\langle c_f \rangle - \langle c_m \rangle) \right], \quad (3.5b)$$

where

$$M_1 = - \left(\frac{\Psi}{6} + \frac{A}{2} + B \right) \quad \text{and} \quad N_1 = \frac{\Psi h}{\lambda^2} - \frac{F}{\lambda} (e^{\lambda h} - 1) + \frac{E}{\lambda} (e^{-\lambda} - 1), \quad (3.6a,b)$$

subject to

$$\langle c_f \rangle(x=0, t) = 1, \quad \langle c_f \rangle(x=\infty, t) = 0, \quad \langle c_f \rangle(x, t=0) = 0, \quad (3.7a-c)$$

$$\frac{\partial \langle c_m \rangle}{\partial x}(x=0, t) = 0, \quad \langle c_m \rangle(x=\infty, t) = 0, \quad \langle c_m \rangle(x, t=0) = 0, \quad (3.8a-c)$$

under the assumption that $\langle c_i^{(1)} \rangle = \langle c_i^{(2)} \rangle = 0$, $i = \{f, m\}$, and provided that the conditions

- (1) $\epsilon \ll 1$,
- (2) $Pe < \epsilon^{-1/2}$

are met. Condition (1) ensures that geometric scale separation exists and is satisfied when the channel is long and thin. Condition (2) provides an upper bound on the Péclet number. To ensure that the higher-order correction terms have zero mean, we set $\langle c_i^{(1)} \rangle = \langle c_i^{(2)} \rangle = 0$ (Mikelic *et al.* 2006).

The advection–dispersion equations (3.5) are coupled through a source term describing the mass exchange between the matrix and the channel. Unlike existing works (Reichert & Wanner 1991; Kazezyilmaz-Alhan 2008), which have postulated the coupling in the form of a storage term only, i.e. $(\langle c_f \rangle - \langle c_m \rangle)$, our analysis demonstrates that an additional contribution due to concentration gradients along the channel, i.e. $\partial \langle c_i \rangle / \partial x$, $i = \{m, f\}$, must be considered as well. We emphasize that the flux $\partial \langle c_m \rangle / \partial x$ is an advective term contributed by the non-zero permeability matrix.

This is different from Tang *et al.* (1981), Dejam *et al.* (2014) or Roubinet *et al.* (2012), who only consider diffusive transport in the porous medium.

In (3.5), D_f^* and D_m^* are the dispersion coefficients for the channel and the matrix respectively. The channel dispersion coefficient D_f^* is defined as

$$D_f^* = D_f + Pe^2 \frac{I_f}{D_f}, \quad (3.9)$$

or, equivalently and without loss of generality,

$$D_f^* = 1 + Pe^2 I_f, \quad (3.10)$$

if $D^* \equiv \tilde{D}_f$ and $D_f \equiv 1$ in (3.2) and (3.9) respectively. In the following, we will use the second expression (3.10) (i.e. $D_f \equiv 1$), as it allows a direct comparison with formulae derived by other authors (Horne & Rodriguez 1983; Griffiths *et al.* 2013; Dejam *et al.* 2014). In (3.10), $I_f = (3/560)\Psi^2 + (1/40)A\Psi + (7/360)B\Psi + (7/240)A^2 + (1/24)AB$, i.e.

$$I_f = \frac{\Psi^2}{105} [1 + g(\lambda, \Lambda)], \quad (3.11)$$

where

$$g(\lambda, \Lambda) = \frac{7}{3} \frac{(e^\Lambda - 1)[e^\Lambda - 1 + \lambda(1 + e^\Lambda)]}{\lambda^2(1 + e^{2\Lambda})}, \quad (3.12)$$

or, equivalently,

$$g(\lambda, \Lambda) = \frac{7}{3\lambda} \left[\tanh\Lambda + \frac{1}{\lambda} (1 - \operatorname{sech}\Lambda) \right]. \quad (3.13)$$

Moreover, from (2.11) it is immediate to show that

$$\frac{U_{slip}}{\Psi} = -\frac{3}{7} g(\lambda, \Lambda), \quad (3.14)$$

i.e. the normalized interfacial velocity $-U_{slip}/\Psi$ is solely controlled by the porous matrix properties.

We emphasize that D_f^* explicitly depends on λ (inverse of the dimensionless permeability) through I_f . The matrix dispersion coefficient is

$$D_m^* = D_{mx} - Pe^2 \frac{I_m}{D_{my}}, \quad (3.15)$$

where

$$I_m = \frac{1}{h} \int_{-h}^0 u_m(y) N(y) dy \quad (3.16)$$

and

$$N(y) = \int_0^y dy' \int_0^{y'} u_m(y^*) dy^*, \quad 0 < y^* < y', \quad 0 < y' < y. \quad (3.17)$$

The derivation details are presented in the [Appendix](#).

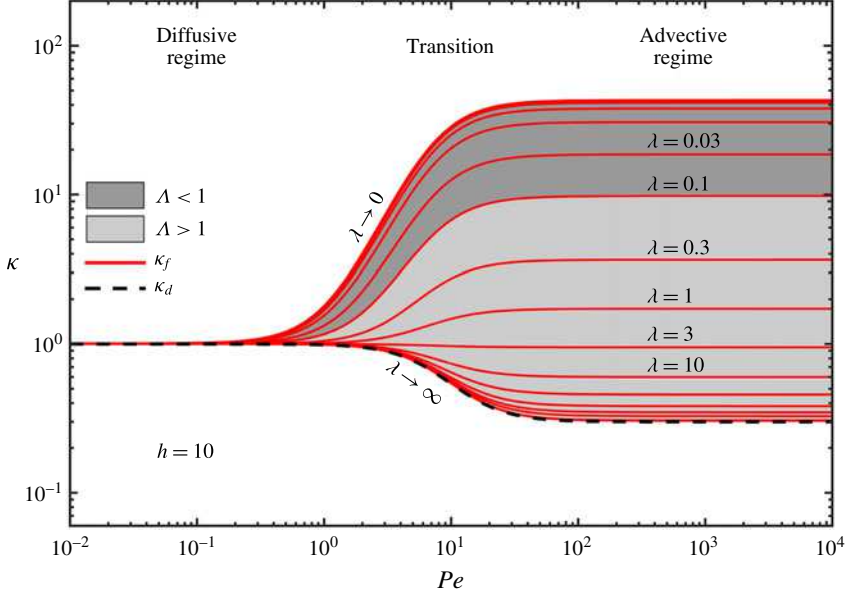


FIGURE 2. (Colour online) Normalized dispersion coefficients κ_f (solid red lines) and κ_d (dashed back line) versus Pe for different values of λ and Λ . Here, $\Psi = -0.78$ and $h = 10$.

4. Dispersion coefficient and matrix properties

In order to investigate the impact of the matrix effective properties, h and λ , on macroscale transport in the channel, we compare D_f^* in (3.10) with the dispersion coefficient D_d obtained by Dejam *et al.* (2014) for a coupled system with purely diffusive transport in the matrix (i.e. $\lambda \rightarrow \infty$ or $k \rightarrow 0$, and $h \neq 0$). To isolate the effect of the width of the porous medium and its permeability, h and λ , on channel macroscopic transport, we normalize both coefficients by the Aris–Taylor dispersion coefficient D_{AT} for a single channel (i.e. $\lambda \rightarrow \infty$ or $k \rightarrow 0$, and $h = 0$) and define

$$\kappa_f := \frac{D_f^*}{D_{AT}} \quad \text{and} \quad \kappa_d := \frac{D_d}{D_{AT}}, \quad (4.1a,b)$$

where (Horne & Rodriguez 1983; Dejam *et al.* 2014)

$$D_d = 1 + \frac{1}{175}Pe^2 \quad \text{and} \quad D_{AT} = 1 + \frac{2}{105}Pe^2. \quad (4.2a,b)$$

In figure 2, we plot κ_f and κ_d as a function of Pe and λ , for a fixed h . The figure shows that two thresholds exist, such that κ_f is constant for $Pe < Pe_{min}$ and $Pe > Pe^*$. For small Péclet number ($Pe < Pe_{min} \approx 1$), $\kappa_f \rightarrow \kappa_d$, i.e. the dispersion coefficient for the coupled system with permeable matrix (finite λ) converges to its non-permeable matrix limit ($\lambda \rightarrow \infty$, $h \neq 0$) independent of h and λ . When $Pe < 1$, advective mixing both in the matrix and in the channel is negligible relative to diffusive mixing. As a result, $\kappa_f \rightarrow \kappa_d$ and $\kappa_d \rightarrow 1$. In the intermediate range of Péclet numbers ($1 < Pe < Pe^*$), κ_f changes from $\kappa_f = 1$ to $\kappa_f = \kappa_f(\lambda, h)$ when $Pe > Pe^*$. It is worth noticing that the dispersion coefficient can overcome its purely diffusive limit when $\lambda < 1$, i.e. mixing

is enhanced compared with a channel of half-width b . When $1 < Pe < Pe^*$, κ_f is a function of Pe , h and λ . Therefore, the matrix properties (or λ and h) and boundary conditions (or Pe) can be independently modified to achieve the desired dispersion coefficient.

As mentioned above, for large Péclet number ($Pe > Pe^*$), κ_f reaches a Pe -independent asymptotic value $\kappa_{\lambda,h}$, i.e. $\lim_{Pe \rightarrow \infty} \kappa_f = \kappa_{\lambda,h}$. In this regime, for any given Pe , the dispersion coefficient increases with decreasing λ (figure 2). This phenomenon is attributed to a decreasing mass flux at the interface between the channel and the matrix, and a resulting decreasing mass loss towards the matrix. Such mass loss is smaller compared with the zero-permeability case, where no solute is transported from the upper steam by the flow in the matrix. This is a newly identified mechanism regulating mass exchange between the channel and the matrix, which is purely controlled by the matrix properties (λ and h) at fixed operating conditions (i.e. constant Péclet number). This mechanism is different from the mass transfer mechanism first proposed by Wu, Ye & Sudicky (2010) and then quantified by Dejam *et al.* (2014), where the channel–matrix interface flux increases (and the dimensionless dispersion coefficient κ_d decreases) with increasing Péclet number and is independent of the matrix properties λ and h . In the zero-permeability limit, i.e. $\lambda \rightarrow \infty$, and for fixed Pe , $\kappa_f \rightarrow \kappa_d$, as expected. In the following, we focus on the study of the dispersion coefficient in the matrix, κ_f , only, since it is deemed more relevant to many engineering applications where transverse mixing enhancement in the channel is the primary target.

We aim to identify the scaling behaviour of κ_f in different regimes, if it exists. Combining (3.11) and (3.10) with (4.1) leads to

$$\kappa_f = 105 \frac{1 + Pe^2 I_f}{105 + 2Pe^2}, \quad (4.3)$$

with I_f given by (3.11). We define $\kappa_{f,Pe \rightarrow 0}$ and $\kappa_{f,\lambda \rightarrow \infty}$ as the fracture dimensionless dispersion coefficients in the two purely diffusive limits: $Pe \rightarrow 0$ for any λ , and $\lambda \rightarrow \infty$ for any Pe respectively. The coefficient $\kappa_{f,Pe \rightarrow 0}$ corresponds to the scenario where mass transport in the matrix is driven solely by diffusion since $Pe = 0$; $\kappa_{f,\lambda \rightarrow \infty}$ corresponds to the case of diffusive transport in an impermeable matrix. The latter differs from Aris–Taylor dispersion in that the channel–porous interface is impermeable to flow, but permeable to mass. If $Pe \rightarrow 0$, $D_f^* = 1$ and

$$\kappa_{f,Pe \rightarrow 0} := \frac{\lim_{Pe \rightarrow 0} D_f^*}{D_{AT}} = \frac{105}{105 + 2Pe^2}. \quad (4.4)$$

Since $\Lambda \rightarrow \infty$ when $\lambda \rightarrow \infty$ for $h \neq 0$, then

$$\kappa_{f,\lambda \rightarrow \infty} := \frac{\lim_{\lambda \rightarrow \infty} D_f^*}{D_{AT}} = \frac{105 + Pe^2 \Psi^2}{105 + 2Pe^2}. \quad (4.5)$$

Combining (4.4) and (4.5) with (4.3) leads to the following expression for κ_f :

$$\kappa_f = \kappa_{f,Pe \rightarrow 0} + g(\Lambda, \lambda) \cdot (\kappa_{f,\lambda \rightarrow \infty} - \kappa_{f,Pe \rightarrow 0}), \quad (4.6)$$

where $g(\Lambda, h)$ is defined in (3.13). In order to isolate the dependence of κ_f from the matrix properties, λ and h , we define the normalized dimensionless dispersion coefficient Π ,

$$\Pi := \frac{\kappa_f - \kappa_{f,Pe \rightarrow 0}}{\kappa_{f,\lambda \rightarrow \infty} - \kappa_{f,Pe \rightarrow 0}}, \quad (4.7)$$

which satisfies

$$\Pi = g(\Lambda, \lambda) = -\frac{7}{3} \frac{U_{slip}}{\Psi}, \quad (4.8)$$

i.e. it is independent of Pe . It is worth noticing that Π scales as U_{slip} normalized by Ψ . In figure 2, κ_f reaches a Pe -independent threshold when $Pe \rightarrow \infty$. Since $\lim_{Pe \rightarrow \infty}(\kappa_{f, Pe \rightarrow 0}) = 0$ and $\lim_{Pe \rightarrow \infty}(\kappa_{f, \lambda \rightarrow \infty}) = \Psi^2/2$, then

$$\lim_{Pe \rightarrow \infty} \kappa_f \sim \lim_{Pe \rightarrow \infty} \Pi. \quad (4.9)$$

From (4.8), we obtain

$$\kappa_f^{threshold} = \lim_{Pe \rightarrow \infty} \kappa_f = -\frac{7\Psi}{6} U_{slip} = \frac{\Psi^2}{2} \Pi, \quad (4.10)$$

i.e. in the advective limit the dispersion coefficient is controlled by the slip velocity at the interface between the porous matrix and the channel.

In the following, we study the scaling behaviour of Π (or U_{slip}/Ψ) for thin ($\Lambda \ll 1$) and thick ($\Lambda \gg 1$) porous matrices.

4.1. Thin porous matrix limit, $\Lambda \ll 1$

The asymptotic expansion of (4.8) about $\Lambda = 0$ leads to

$$\Pi = \frac{7}{3} \left[\left(h + \frac{h^2}{2} \right) - \left(\frac{h}{3} + \frac{5h^2}{24} \right) \Lambda^2 + O(\Lambda^5) \right], \quad (4.11)$$

since $\tanh \Lambda \approx \Lambda - \Lambda^3/3 + O(\Lambda^5)$ and $\operatorname{sech} \Lambda \approx 1 - \Lambda^2/2 + 5\Lambda^4/24 + O(\Lambda^6)$. Retaining the leading-order term, we obtain

$$\Pi \sim h \left(1 + \frac{h}{2} \right), \quad \text{for } \Lambda \ll 1, \quad (4.12)$$

which shows that the dispersion is controlled by the matrix thickness h for thin porous layers. Figure 3(a) shows the scaling behaviour of $\Pi(h^2 + 2h)^{-1}$ versus Λ and suggests that the scaling (4.12) is a valid approximation for $\Lambda \rightarrow 1$ as well, i.e.

$$\Pi \sim h \left(1 + \frac{h}{2} \right), \quad \text{for } \Lambda \lesssim 1. \quad (4.13)$$

Further, two scaling regimes exist for $h \ll 1$ and $h \gg 1$, i.e.

$$\Pi \sim h, \quad \text{for } \Lambda \lesssim 1, h \ll 1 \quad (4.14a)$$

$$\Pi \sim h^2, \quad \text{for } \Lambda \lesssim 1, h \gg 1. \quad (4.14b)$$

In figure 3(b), we plot Πh^{-1} as a function of h for different $\Lambda \in [0.001, 1]$. As expected, Πh^{-1} is constant when $h \ll 1$ and grows linearly with h when $h \gg 1$. This result suggests that transverse mixing in a channel with a thin porous coating ($\Lambda \ll 1$) is controlled by h , and is more sensitive to the matrix width when $h \gg 1$, i.e. for a given increase in H , ΔH , better mixing can be achieved if $H > b$.

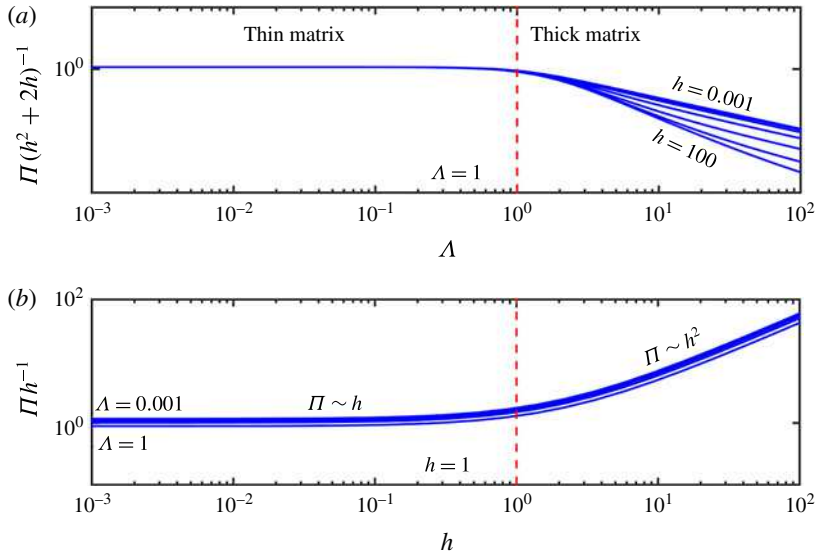


FIGURE 3. (Colour online) (a) Scaling behaviour of the normalized dispersion coefficient Π defined in (4.7) for thin porous media ($\Lambda \lesssim 1$) and (b) $h < 1$ and $h > 1$. The coefficient Π , i.e. transverse dispersion, is controlled by the width h of the porous matrix when $\Lambda \lesssim 1$; this dependence goes from linear to quadratic as h increases above the threshold $h \approx 1$.

4.2. Thick porous matrix limit, $\Lambda \gg 1$

In the limit $\Lambda \gg 1$, i.e. for thick porous matrices, we expand (4.8) about $1/\Lambda = 0$ and obtain

$$\Pi = \frac{7}{3} \frac{(h\Lambda^{-1} + h^2\Lambda^{-2})e^{2\Lambda} - h^2\Lambda^{-2}e^\Lambda - h\Lambda^{-1}}{1 + e^{2\Lambda}} + O(\Lambda^{-2}), \quad (4.15)$$

since $e^\Lambda(1 + e^{2\Lambda})^{-1} \rightarrow 0$ and $e^{2\Lambda}(1 + e^{2\Lambda})^{-1} \rightarrow 1$ when $\Lambda \rightarrow \infty$. At the leading order,

$$\Pi \sim \frac{1}{\lambda}, \quad \text{for } \Lambda \gg 1, \quad (4.16)$$

i.e. the normalized dispersion is controlled by the matrix permeability only. Figure 4 shows that $\Pi\lambda$ reaches a Λ -independent value for $\Lambda \gg 1$, as suggested by (4.16). This analysis shows that when increasing the thickness of the matrix for a given λ , further increments of h will no longer affect the slip velocity when $\Lambda \gg 1$. In this regime, the bottom wall of the matrix (located at $y = -h$) becomes ‘invisible’ to the flow and transport in the channel, and changes in h will not influence the channel dynamics. For a given channel–matrix system with $\Lambda \gg 1$, an effective control of the dispersion can be achieved by modifying the permeability of the porous medium.

5. Validation and model accuracy: numerical experiments

The system (3.5) is composed of two one-dimensional transient coupled upscaled equations. The coupling is due to the mass exchange at the interface between the channel and the matrix. Here, we solve the coupled system (3.5) numerically. We test the accuracy of the upscaling approximation (3.5a) and (3.5b) by comparison with the averaged 2D solution obtained from numerically solving (2.18a) and (2.18b).

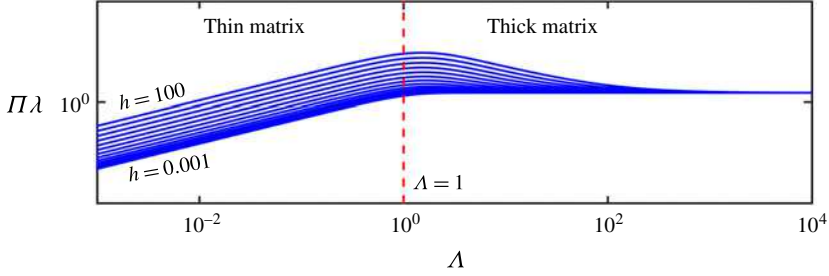


FIGURE 4. (Colour online) Scaling behaviour of the normalized dispersion coefficient Π defined in (4.7) for thick porous media ($\Lambda \gg 1$). The normalized dispersion coefficient is controlled by the matrix permeability only when $\Lambda \gg 1$.

5.1. Code validation

For the discretization of the 1D equations (3.5), we use implicit Euler in time and second-order central finite difference discretization in space. For the 2D equations (2.18), we use backward Euler for the time discretization and second-order discretization in space, with upwinding for the advective term and central finite differences for the other terms. A convergence study is performed on the 1D solver by refining the grid size and time step. We validate the 2D solver by setting $\phi = 1$, $D_f = D_{mx} = D_{my}$ and $u_f = u_m = u^*$ in (2.18). This corresponds to passive transport in a single channel (and no porous medium) with uniform velocity u^* for which a closed-form analytical solution is available (Ogata & Banks 1961). We compare the numerical average of the pore-scale concentration c_f with the analytical solution for the continuous injection of a passive solute. The mean concentration profile satisfies (Ogata & Banks 1961)

$$\langle c_f \rangle(x, t) = \frac{1}{2} \left[\operatorname{erfc} \left(\frac{x - u^* t}{2\sqrt{D_f t}} \right) + \exp \left(\frac{u^* x}{D_f} \right) \operatorname{erfc} \left(\frac{x + u^* t}{2\sqrt{D_f t}} \right) \right]. \quad (5.1)$$

Figure 5 shows the match between the numerically upscaled 2D concentration and the analytical solution (5.1).

5.2. Upscaled model accuracy and predictivity

We verify the accuracy of the upscaling procedure by comparing the macroscale concentrations $\langle c_f \rangle_{1D}$ and $\langle c_m \rangle_{1D}$ obtained from (3.5) with the numerical averages of the microscale two-dimensional concentrations obtained from (2.18), $\langle c_f \rangle_{2D}$ and $\langle c_m \rangle_{2D}$. The upscaled model (3.5) is considered to be predictive of pore-scale behaviour if the absolute error between upscaled and microscale quantities is bounded by $\sqrt{\epsilon}$, as prescribed by the homogenization procedure. All parameters in the 2D pore-scale equations are uniquely mapped onto the effective parameters of the corresponding macroscopic system.

Without loss of generality, we consider a continuous injection at the channel inlet, i.e. $c_f(x=0, y, t) = 1$ and $\partial_x c_m(x=0, y, t) = 0$. This corresponds to the inlet boundary conditions $\langle c_f \rangle(x=0, t) = 1$ and $\partial_x \langle c_m \rangle(x=0, t) = 0$ in the upscaled model.

In figure 6, we compare the averaged fully resolved two-dimensional and the upscaled approximated solutions $\langle c_f \rangle_{2D}(x, t)$ and $\langle c_f \rangle_{1D}(x, t)$ respectively for different

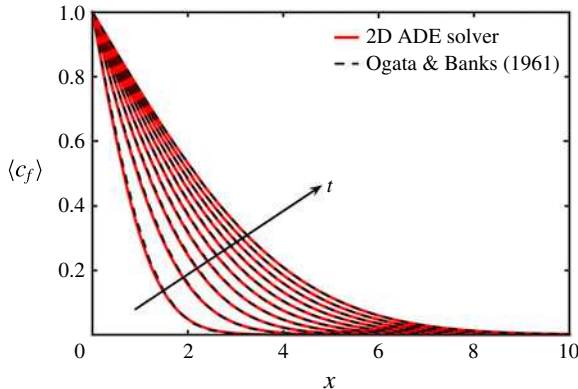


FIGURE 5. (Colour online) Comparison between the averaged 2D concentration in the channel and the 1D analytical solution, equation (5.1) (Ogata & Banks 1961), for passive scalar transport in a single channel with uniform velocity and constant injection. The average concentration $\langle c_f \rangle$ is plotted in terms of the dimensionless distance from the channel inlet at different instances in time \tilde{t} . Here, $h = 10$, $\phi = 1$, $\epsilon = 0.01$, $D_f = D_{mx} = D_{my} = 1$ and $u_f = u_m = u^* = 0.01$.

values of the Péclet number, $Pe = \{0.1, 10, 100, 1000\}$, and porosity, $\phi = \{0.01, 0.1\}$, and plot the absolute error $E_f(x, t) := |\langle c_f \rangle_{2D} - \langle c_f \rangle_{1D}|$. The simulations in figure 6 are run for $\epsilon = 0.02$, $\lambda = 10$ and $\phi = 0.1$.

In figure 6, we show that the absolute error between the 2D and 1D models decreases with increasing time and distance from the inlet for all scenarios. More specifically, the macroscopic 1D model performs within the expected accuracy for $Pe < \epsilon^{-1/2}$ (≈ 7 for $\epsilon = 0.02$), i.e. $E_f(x, t)$ is bounded by $\sqrt{\epsilon}$, see figure 6(d,h). The error bound is satisfied even when the constraints on the Péclet number are relaxed, i.e. $O(\epsilon^{-1/2}) \leq Pe \leq O(\epsilon^{-1})$, or $10 \leq Pe \leq Pe^*$ in figures 6(b,f) and (c,g). This result highlights that the conditions (1) and (2) are sufficient, but not necessary, to guarantee that error bounds prescribed by homogenization theory are realized. For $Pe > O(\epsilon^{-1})$ (or $Pe > Pe^*$), $E_f(x, t) > \sqrt{\epsilon}$ for early times; the 1D model regains its accuracy at late (dimensionless) times $t > \epsilon Pe$, i.e. $t > 20$ in figure 6(a,e).

In figure 7, we plot the profiles of the average concentration in the channel obtained from the numerically averaged 2D equations and the 1D upscaled equations. The simulations are run for $\lambda = 31.6$ and $\phi = 0.1$. The error between the microscale and macroscale equations, figure 7(b), is lower compared with the scenario with the same Péclet number and higher permeability and porosity, specifically figure 6(c,g). This is consistent with the upscaling approach, where higher-order terms in the transverse direction are neglected, thus leading to increased error for a highly permeable matrix.

To further investigate the accuracy of the upscaled equations in different regimes and the temporal dependence of the error, we plot the solute breakthrough curves at a given location $x = x^*$ along the channel.

In figure 8, we plot the concentration profile for three Péclet numbers and two values of the dimensionless permeability, $\lambda = \sqrt{10^2}$ and $\lambda = \sqrt{10^3}$. For $Pe \ll 1$, there is an excellent agreement between the upscaled and two-dimensional solutions for all times and both permeability values. The match is within the expected error bounds, figure 8(a). For higher Péclet numbers, $Pe = 1$ (figure 8b) and $Pe = 1000$ (figure 8c), the upscaled solution can still capture the averaged pore-scale concentration despite

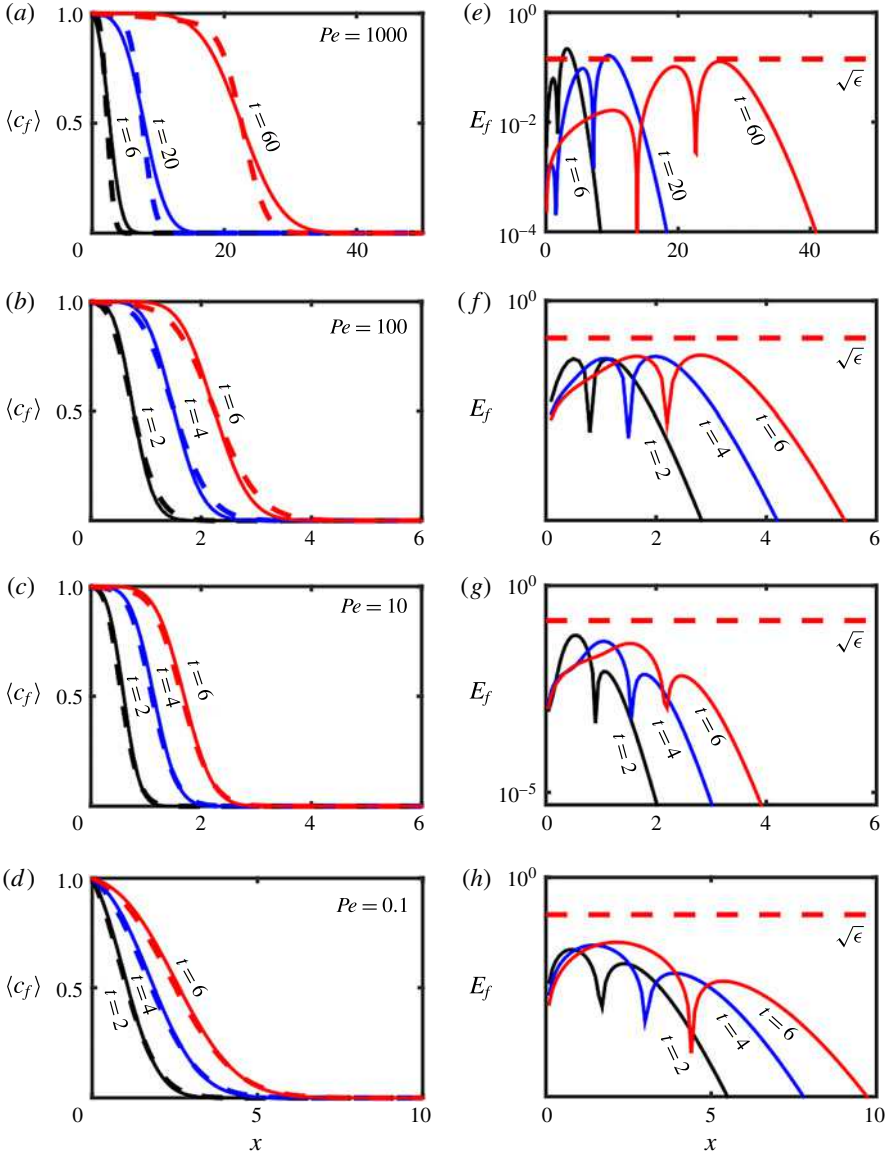


FIGURE 6. (Colour online) (a–d) Average concentration profiles $\langle c_f \rangle$ along the channel obtained either from the upscaled 1D (solid lines) or the pore-scale 2D equations (dashed lines) for different instances in time and Péclet numbers, i.e. $Pe = \{0.1, 10, 100, 1000\}$. (e–h) Absolute error $E_f(x, t) := |\langle c_f \rangle_{2D} - \langle c_f \rangle_{1D}|$ corresponding to each simulation. The dashed horizontal line represents the error bound $\sqrt{\epsilon}$ prescribed by homogenization theory. As predicted, the 1D equations capture the pore-scale dynamics within errors of order $\sqrt{\epsilon}$ for $Pe < \epsilon^{-1/2} \approx 7$. Importantly, for $10 < Pe < 100$, the 1D simulation is still accurate. For $Pe = 1000$, the error is not bounded by $\sqrt{\epsilon}$ at early times, but the 1D model accuracy is recovered at later times. The simulation parameters are $\epsilon = 0.02$, $\lambda = 10$, $\Psi = -0.78$, $\phi = 0.1$, $D_f = 1$, $D_{mx} = 0.1$, $D_{my} = 0.1$ and $h = 10$.

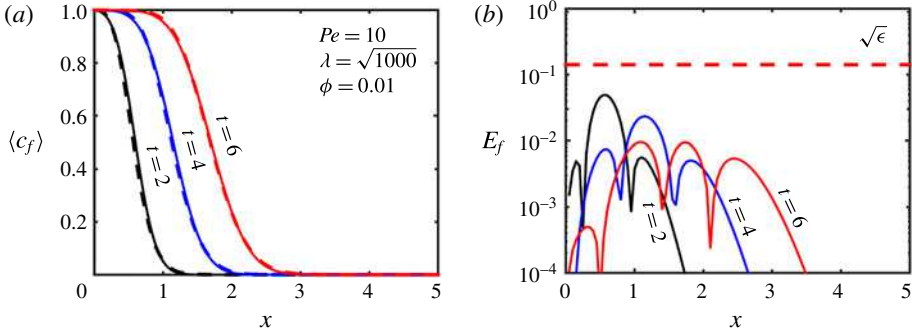


FIGURE 7. (Colour online) Simulation parameters: $\epsilon = 0.02$, $\lambda = 31.6$, $\phi = 0.1$, $\Psi = -0.78$, $D_f = 1$, $D_{mx} = 0.1$, $D_{my} = 0.1$, $h = 10$. (a) Average concentration profiles $\langle c_f \rangle$ along the channel obtained either from the upscaled 1D (solid lines) or from the pore-scale 2D equations (dashed lines) for different instances in time. (b) Absolute error $E_f(x, t) := |\langle c_f \rangle_{2D} - \langle c_f \rangle_{1D}|$ corresponding to each simulation. The dashed horizontal line represents the error bound $\sqrt{\epsilon}$ prescribed by homogenization theory.

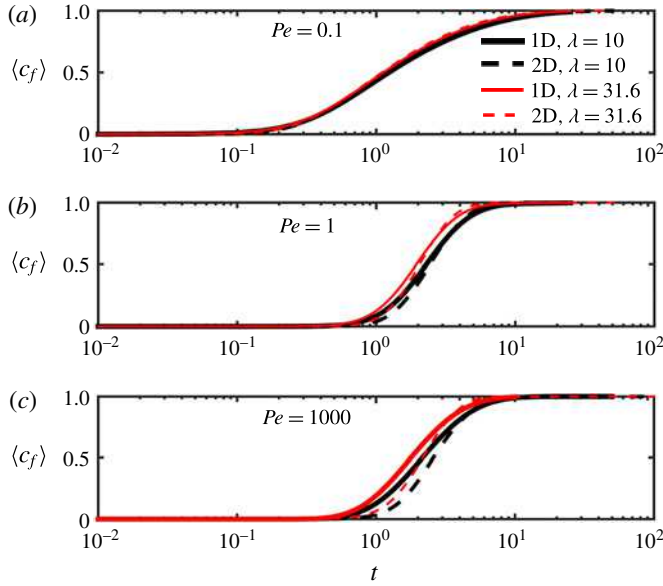


FIGURE 8. (Colour online) Time evolution of the channel average concentration $\langle c_f \rangle$ calculated at location $x^* = b$ for different λ and Péclet numbers. The parameters used in the simulations are $\phi = 0.01$, $\Psi = -0.78$, $\epsilon = 0.01$, $D_f = 1$ and $h = 10$.

the fact that condition (2) is violated for $Pe = 1000$. Good performance of the model in regimes where (2) is violated can be expected since such a constraint is simply a sufficient (and not necessary) condition to guarantee that the upscaled equation (3.5) describes spatially averaged pore-scale processes within errors of order $\sqrt{\epsilon}$. For $Pe = 1000$ the match between the upscaled and the averaged pore-scale solution improves at later times. Since condition (2) is violated, the transient terms in the expansion, specifically $\partial_t c_f^{(0)}$ and $\partial_t c_m^{(0)}$ in (A 3a), are not negligible and should be accounted for

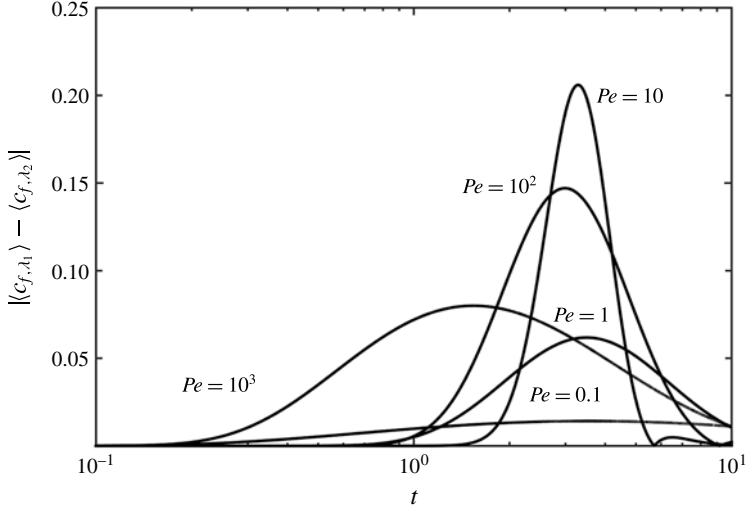


FIGURE 9. Difference between the average concentration in the channel $\langle c_f \rangle$ for two values of the dimensionless permeability, $\lambda = \sqrt{10^2}$ and $\lambda = \sqrt{10^3}$, and different Péclet numbers, obtained from (3.5). The set of parameters used in the simulations is $\phi = 0.5$, $\Psi = -0.78$, $\epsilon = 0.02$, $D_f = 1$, $D_{mx} = 0.1$, $D_{my} = 0.1$, $h = 10$. The concentration $\langle c_f \rangle$ is measured at $x = 1$.

at the leading order. Failing to do so yields to a slightly higher approximation error, which decreases in time as the solution approaches the steady state and the transient terms become increasingly small, i.e. $\partial_t c_f^{(0)} \rightarrow 0$ and $\partial_t c_m^{(0)} \rightarrow 0$ as $t \rightarrow \infty$.

5.3. Upscaled model results

Figure 9 shows the difference between the average concentrations in the channel calculated from (3.5) for two values of λ , $\lambda = \sqrt{10^2}$ and $\lambda = \sqrt{10^3}$, at a given location along the channel, and for different Péclet numbers. Figure 9 shows how differences in matrix permeability become more relevant for intermediate Péclet numbers, i.e. $Pe \in (1, Pe^*)$, when the interplay between advective and diffusive mass transfer is strongly controlled by the matrix properties. For $Pe < 1$, diffusive transport is dominant. In this scenario, the geometrical characteristics of the matrix have a small impact on transport. Similarly, for $Pe > Pe^*$, the impact of the matrix permeability decreases. In advection-dominated regimes, the concentration reaches saturation ($c_f = 1$) in a short period of time. This leads to a weak dependence of the macroscale concentration on the matrix topological features.

Figure 10 shows the temporal evolution of the macroscopic concentration in the channel and the matrix at a given location along the flow direction. In diffusion-dominated regimes, i.e. when $Pe < 1$, figure 10(a), the concentration difference in the matrix and the channel is very small. Fast diffusive mass transport enhances transverse mixing at the interface between the matrix and the channel, and leads to decreased differences in concentration between the former and the latter. For high Péclet numbers, figure 10(b), the difference in the average concentrations in the matrix and the channel increases due to the delay in advective mass transfer in the matrix. As a result, the concentration gradient, and therefore the mass flux, across the matrix–channel interface increases with Pe for a given permeability value.

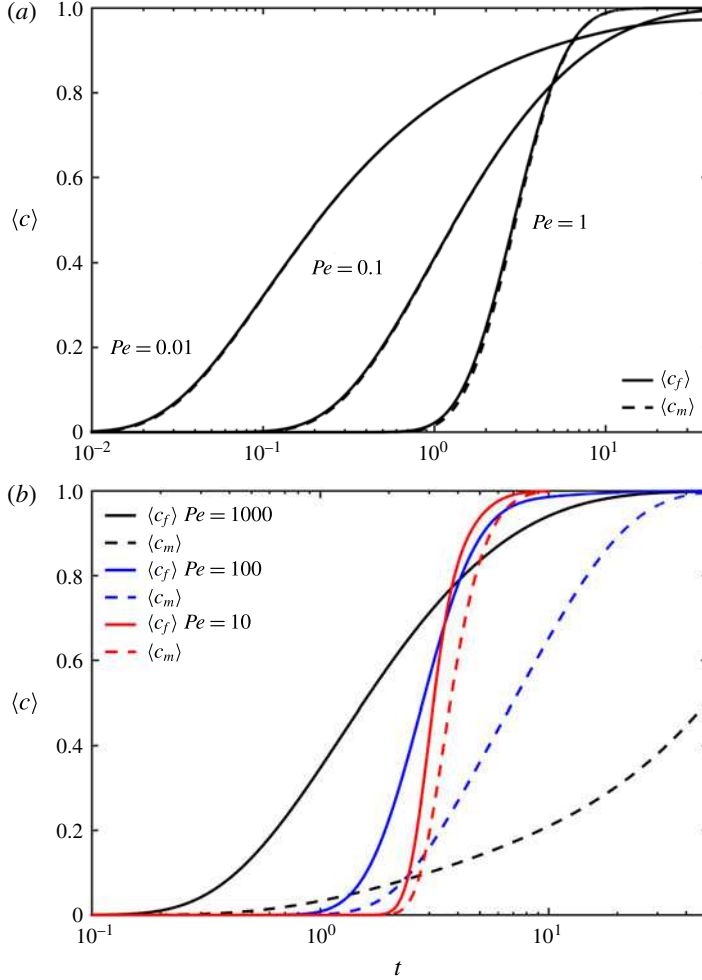


FIGURE 10. (Colour online) Comparison between $\langle c_f \rangle$ (solid lines) and $\langle c_m \rangle$ (dashed lines) for low (a) and high Péclet numbers (b). The simulation parameters are $\phi = 0.5$, $\Psi = -0.78$, $\epsilon = 0.02$, $D_f = 1$, $D_{mx} = 0.1$, $D_{my} = 0.1$, $h = 10$. The concentrations $\langle c_f \rangle$ and $\langle c_m \rangle$ are measured at $x = 1$.

5.4. Comparison with existing models

In this section, we compare the proposed model with that introduced by Dejam *et al.*, who assume that mass transport in the porous matrix is purely diffusive and transverse to flow (i.e. y -direction). This corresponds to the $k = 0$ (or $\lambda \rightarrow \infty$) limit in the present model. To analyse differences and/or similarities in performance between the two models, we consider two configurations: a highly permeable ($\lambda = 0.3$) and a nearly impermeable ($\lambda = 100$) matrix. Dejam *et al.*'s solution for the average concentration in the fracture, $\langle c \rangle_{f,DHC}$, is (Dejam *et al.* 2014)

$$\langle c \rangle_{f,DHC}(x, t_D) = \frac{e^{\alpha t_D}}{t_D} \left\{ \frac{1}{2} \hat{C}_{f,DHC}(x, \alpha) + Re \left[\sum_{l=1}^n (-1)^l \hat{C}_{f,DHC} \left(x, \alpha + \frac{l\pi}{t_D} \sqrt{-1} \right) \right] \right\}, \quad (5.2)$$

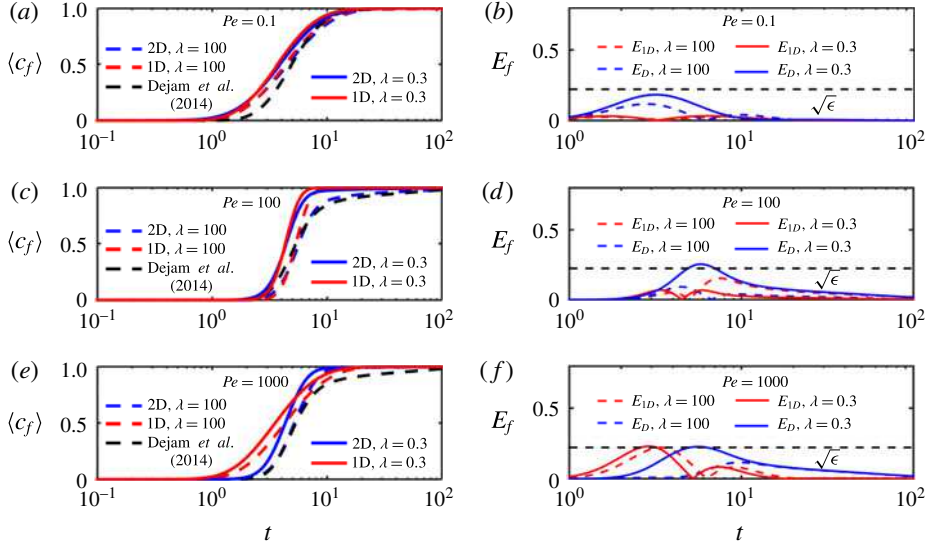


FIGURE 11. (Colour online) (a,c,e) Comparison between the breakthrough curves obtained from (3.5a) and (5.2) (by Dejam *et al.*) and the averaged pore-scale solution for two permeability values, $\lambda = 0.3$ and $\lambda = 100$. (b,d,f) Absolute errors between the upscaled solutions (3.5a) and (5.2) and the averaged pore-scale solution, $E_{1D}(x, t; \lambda) := |\langle c_f \rangle_{2D} - \langle c_f \rangle_{1D}|$ and $E_D(x, t; \lambda) := |\langle c_f \rangle_{2D} - \langle c_f \rangle_{f, Dejam \text{ et al.}}|$ respectively. The simulation parameters are $\epsilon = 0.02$, $\phi = 0.1$, $\Psi = -1$, $D_f = 1$, $D_{mx} = 0.1$, $D_{my} = 0.01$ and $h = 10$.

where $Re[\cdot]$ represents the real part of a complex function, α controls the accuracy of the numerical Laplace transform and $t_D = \tilde{t}/(b^2/D_{my})$. In the following comparative study, we use the dimensionless time defined in (3.2) instead. Moreover, we set $\alpha t_D = 4$ and use $n = 1e5$ terms in the summation.

In figure 11, we compare the models (3.5a) and (5.2) (by Dejam *et al.*) with the macroscopic concentration obtained from averaging the pore-scale solution. For low Péclet numbers, both models perform well independently of the matrix permeability. For high Péclet number ($Pe = 100$) and low permeability (or high λ), Dejam *et al.*'s solution shows a better accuracy than the upscaled model proposed here. This is apparent from the error E_f plotted in figure 11 as a function of time: while model (3.5a) can still be considered to be predictive since E_f is bounded by $\sqrt{\epsilon}$, Dejam *et al.*'s solution has a lower maximum error. Conversely, for $Pe = 100$ and high permeability values (or low λ), our upscaled equation (3.5a) is more accurate than (5.2). Importantly, in this scenario, the error in Dejam *et al.*'s solution is not bounded by $\sqrt{\epsilon}$, i.e. the error is larger than that prescribed by the upscaling procedure. Finally, for very large Pe ($Pe = 1000$), both models give higher errors at early times, regardless of the permeability value. This analysis demonstrates that the model described by (3.5a) and Dejam *et al.*'s solution are complementary to each other, since the former can accurately describe macroscopic mass transport in advection-dominated regimes in coupled systems with highly permeable matrices, while the latter captures transverse diffusion into the matrix only in the low-permeability case.

6. Conclusions

Flow and transport above micro-patterned and porous surfaces occur in a variety of systems, ranging from engineered surfaces to bioreactor devices. The achievement of optimal macroscopic properties, e.g. improved mixing, in a number of such applications is hampered by the lack of understanding of how surface/matrix properties (e.g. porosity, permeability and thickness) relate to the system or macroscale.

In this work, we use perturbation methods to study passive scalar transport in a coupled channel–matrix system and obtain an analytical relationship between matrix properties and solute transverse dispersion. To the best of our knowledge, this is the first analytical relationship that establishes a connection between macroscopic transport features, matrix properties and transport regimes (i.e. Péclet number). We accomplish this by deriving upscaled equations for mass transport in a channel–matrix coupled system, while accounting for two-dimensional diffusion and a non-uniform velocity field both in the channel and in the matrix. The average velocity profile in the coupled system, as well as the slip velocity at the channel–matrix interface, is determined by a two-domain approach where the Stokes and Darcy–Brinkman equations are coupled to describe flow in the channel and in the permeable matrix respectively.

Our results show that the impact of matrix properties on solute transverse mixing, and, more specifically, on the macroscopic dispersion coefficient, is controlled by the magnitude of the Péclet number. In particular, for $Pe < 1$, transport in the channel–matrix system is dominated by diffusion, and the matrix properties have little to no impact on macroscopic transport. In this regime, mixing is controlled by diffusion in the direction transverse to the mean flow, and the dimensionless dispersion coefficient is independent of both Pe and the matrix permeability. When $1 < Pe < Pe^*$, solute transport is controlled by both diffusion and advection. The interplay between these mass transport mechanisms is strongly dependent on both the matrix permeability and the Péclet number. In this regime, macroscale dispersion can be controlled by both active and passive mechanisms. The former consist in modifying the operating flow conditions of the device (i.e. Péclet number), while the latter are based on modifying the surface coating properties (i.e. permeability). For $Pe > Pe^*$, mass transport is dominated by advection, and the dispersion coefficient reaches a constant value independent of the Péclet number and a function of the matrix permeability only. By means of asymptotic analysis, we demonstrate that different scaling regimes of the normalized dispersion coefficient Π exist for thin ($\Lambda \lesssim 1$) and thick porous layers ($\Lambda \gg 1$). In particular, Π is controlled by the dimensionless width h of the porous matrix, when $\Lambda \lesssim 1$, and scales linearly or quadratically with h , when $h < 1$ or $h > 1$ respectively. In the thick-porous-medium regime, Π is controlled by the matrix permeability λ . This provides specific design guidelines to optimize mixing in channel–porous systems.

The upscaled model was validated against numerical simulations of the fully resolved two-dimensional channel–matrix coupled system. The upscaled solution agrees with the average concentration obtained from the exact two-dimensional ADEs within the error bound prescribed by the homogenization approach and performs well for large Pe , despite the fact that condition (2) is violated. This is to be expected since the latter is a sufficient (and not necessary) condition to guarantee that the upscaled equation (3.5) describes spatially averaged pore-scale processes within errors of order $\sqrt{\epsilon}$.

Finally, a detailed comparison between our model and that of Dejam *et al.* (2014), which only considers one-dimensional transverse diffusion in the matrix, shows that the two models are complementary to each other. For systems with permeable

matrices, we found our model to be superior to Dejam *et al.*'s for all considered Péclet numbers. Conversely, unlike Dejam *et al.*'s model, our model cannot accurately capture the tailing effect introduced by the purely diffuse interfacial mass flux in impermeable matrices.

To the best of our knowledge, this is the first study that provides (i) a rigorous basis to relate the matrix permeability to the dispersion coefficient in coupled channel–matrix systems and (ii) quantitative guidelines for the design of porous/micro-patterned surfaces. The analysis also shows the possibility of controlling dispersion by either active (i.e. changing the operating conditions) or passive mechanisms (i.e. controlling the matrix properties) in the appropriate range of Péclet numbers.

Acknowledgements

I.B. gratefully acknowledges partial support by the US Department of Energy (DOE), Office of Biological and Environmental Research, Subsurface Biogeochemical Research (SBR) Program through the SBR Scientific Focus Area at PNNL, and the National Science Foundation (NSF) through the award no. 1533874, ‘DMREF: an integrated multiscale modelling and experimental approach to design fouling resistant membranes’. A.M.T. was partially supported by the US Department of Energy (DOE) Office of Advanced Scientific Computing (ASCR) as part of the Early Career Award ‘New Dimension Reduction Methods and Scalable Algorithms for Multiscale Nonlinear Phenomena’ and DOE’s Office of Biological and Environmental Research (BER) through the Pacific Northwest National Laboratory (PNNL) Subsurface Biogeochemical Research Scientific Focus Area project. PNNL is operated by Battelle for the DOE under Contract DE-AC05-76RL01830.

Appendix A. Asymptotic expansion

Substituting (3.4) into (3.2a) and (3.2b) leads to

$$\begin{aligned} & \epsilon^{1-\alpha} \left(\frac{\partial c_f^{(0)}}{\partial t} + \sqrt{\epsilon} \frac{\partial c_f^{(1)}}{\partial t} + \epsilon \frac{\partial c_f^{(2)}}{\partial t} \right) + \epsilon^{1/2-\alpha} \left(u_f \frac{\partial c_f^{(0)}}{\partial \xi} + \sqrt{\epsilon} u_f \frac{\partial c_f^{(1)}}{\partial \xi} + \epsilon u_f \frac{\partial c_f^{(2)}}{\partial \xi} \right) \\ & = \epsilon D_f \left(\frac{\partial^2 c_f^{(0)}}{\partial \xi^2} + \sqrt{\epsilon} \frac{\partial^2 c_f^{(1)}}{\partial \xi^2} + \epsilon \frac{\partial^2 c_f^{(2)}}{\partial \xi^2} \right) + D_f \left(\sqrt{\epsilon} \frac{\partial^2 c_f^{(1)}}{\partial y^2} + \epsilon \frac{\partial^2 c_f^{(2)}}{\partial y^2} \right) \end{aligned} \quad (\text{A } 1)$$

and

$$\begin{aligned} & \epsilon^{1-\alpha} \left(\frac{\partial c_m^{(0)}}{\partial t} + \sqrt{\epsilon} \frac{\partial c_m^{(1)}}{\partial t} + \epsilon \frac{\partial c_m^{(2)}}{\partial t} \right) + \epsilon^{1/2-\alpha} \left(u_m \frac{\partial c_m^{(0)}}{\partial \xi} + \sqrt{\epsilon} u_m \frac{\partial c_m^{(1)}}{\partial \xi} + \epsilon u_m \frac{\partial c_m^{(2)}}{\partial \xi} \right) \\ & = \epsilon D_{mx} \left(\frac{\partial^2 c_m^{(0)}}{\partial \xi^2} + \sqrt{\epsilon} \frac{\partial^2 c_m^{(1)}}{\partial \xi^2} + \epsilon \frac{\partial^2 c_m^{(2)}}{\partial \xi^2} \right) + D_{my} \left(\sqrt{\epsilon} \frac{\partial^2 c_m^{(1)}}{\partial y^2} + \epsilon \frac{\partial^2 c_m^{(2)}}{\partial y^2} \right) \end{aligned} \quad (\text{A } 2)$$

respectively. Given $\alpha < 1/2$, we collect terms of like power of ϵ as follows:

$$\begin{aligned} & \sqrt{\epsilon} \left(\epsilon^{-\alpha} u_f \frac{\partial c_f^{(0)}}{\partial \xi} - D_f \frac{\partial^2 c_f^{(1)}}{\partial y^2} \right) + \epsilon \left(\epsilon^{-\alpha} \frac{\partial c_f^{(0)}}{\partial t} + \epsilon^{-\alpha} u_f \frac{\partial c_f^{(1)}}{\partial \xi} - D_f \frac{\partial^2 c_f^{(0)}}{\partial \xi^2} - D_f \frac{\partial^2 c_f^{(2)}}{\partial y^2} \right) \\ & + \epsilon \sqrt{\epsilon} \left(\epsilon^{-\alpha} \frac{\partial c_f^{(1)}}{\partial t} + \epsilon^{-\alpha} u_f \frac{\partial c_f^{(2)}}{\partial \xi} - D_f \frac{\partial^2 c_f^{(1)}}{\partial \xi^2} \right) = O(\epsilon^2), \end{aligned} \quad (\text{A } 3a)$$

$$\begin{aligned}
& \sqrt{\epsilon} \left(\epsilon^{-\alpha} u_m \frac{\partial c_m^{(0)}}{\partial \xi} - D_{my} \frac{\partial^2 c_m^{(1)}}{\partial y^2} \right) \\
& + \epsilon \left(\epsilon^{-\alpha} \frac{\partial c_m^{(0)}}{\partial t} + \epsilon^{-\alpha} u_m \frac{\partial c_m^{(1)}}{\partial \xi} - D_{mx} \frac{\partial^2 c_m^{(0)}}{\partial \xi^2} - D_{my} \frac{\partial^2 c_m^{(2)}}{\partial y^2} \right) \\
& + \epsilon \sqrt{\epsilon} \left(\epsilon^{-\alpha} \frac{\partial c_m^{(1)}}{\partial t} + \epsilon^{-\alpha} u_m \frac{\partial c_m^{(2)}}{\partial \xi} - D_{mx} \frac{\partial^2 c_m^{(1)}}{\partial \xi^2} \right) = O(\epsilon^2). \tag{A 3b}
\end{aligned}$$

Equations (A 3a) and (A 3b) lead to a cascade of equations for the unknown functions $c_j^{(i)}$. Specifically, for $c_f^{(i)}$ and $c_m^{(i)}$ we obtain

$$\frac{\partial^2 c_f^{(1)}}{\partial y^2} = \epsilon^{-\alpha} \frac{u_f}{D_f} \frac{\partial c_f^{(0)}}{\partial \xi}, \tag{A 4a}$$

$$\epsilon^{-\alpha} \frac{\partial c_f^{(0)}}{\partial t} + \epsilon^{-\alpha} u_f \frac{\partial c_f^{(1)}}{\partial \xi} = D_f \frac{\partial^2 c_f^{(0)}}{\partial \xi^2} + D_f \frac{\partial^2 c_f^{(2)}}{\partial y^2}, \tag{A 4b}$$

$$\epsilon^{-\alpha} \frac{\partial c_f^{(1)}}{\partial t} + \epsilon^{-\alpha} u_f \frac{\partial c_f^{(2)}}{\partial \xi} = D_f \frac{\partial^2 c_f^{(1)}}{\partial \xi^2} \tag{A 4c}$$

and

$$\frac{\partial^2 c_m^{(1)}}{\partial y^2} = \epsilon^{-\alpha} \frac{u_m}{D_{my}} \frac{\partial c_m^{(0)}}{\partial \xi}, \tag{A 5a}$$

$$\epsilon^{-\alpha} \frac{\partial c_m^{(0)}}{\partial t} + \epsilon^{-\alpha} u_m \frac{\partial c_m^{(1)}}{\partial \xi} = D_{mx} \frac{\partial^2 c_m^{(0)}}{\partial \xi^2} + D_{my} \frac{\partial^2 c_m^{(2)}}{\partial y^2}, \tag{A 5b}$$

$$\epsilon^{-\alpha} \frac{\partial c_m^{(1)}}{\partial t} + \epsilon^{-\alpha} u_m \frac{\partial c_m^{(2)}}{\partial \xi} = D_{mx} \frac{\partial^2 c_m^{(1)}}{\partial \xi^2} \tag{A 5c}$$

respectively. Expansion of the interface conditions (2.22) yields

$$[c_f^{(0)} + \sqrt{\epsilon} c_f^{(1)} + \epsilon c_f^{(2)}]_{y=0} = [c_m^{(0)} + \sqrt{\epsilon} c_m^{(1)} + \epsilon c_m^{(2)}]_{y=0} \tag{A 6}$$

and

$$\left[\sqrt{\epsilon} \frac{\partial c_f^{(1)}}{\partial y} + \epsilon \frac{\partial c_f^{(2)}}{\partial y} \right]_{y=0} = \left[\sqrt{\epsilon} \frac{\phi D_{my}}{D_f} \frac{\partial c_m^{(1)}}{\partial y} + \epsilon \frac{\phi D_{my}}{D_f} \frac{\partial c_m^{(2)}}{\partial y} \right]_{y=0}. \tag{A 7}$$

Matching like powers of ϵ in (A 7) leads to

$$\left[\frac{\partial c_f^{(1)}}{\partial y} \right]_{y=0} = \frac{\phi D_{my}}{D_f} \left[\frac{\partial c_m^{(1)}}{\partial y} \right]_{y=0}, \tag{A 8}$$

$$\left[\frac{\partial c_f^{(2)}}{\partial y} \right]_{y=0} = \frac{\phi D_{my}}{D_f} \left[\frac{\partial c_m^{(2)}}{\partial y} \right]_{y=0}. \tag{A 9}$$

The cascade of equations (A 3) and (A 4) subject to the boundary conditions (A 6) and (A 8) can be solved iteratively.

Appendix B. Order $O(\sqrt{\epsilon})$: $c_f^{(1)}$ and $c_m^{(1)}$ solutions

Integrating equation (A 4a) with respect to y gives

$$\frac{\partial c_f^{(1)}}{\partial y} = \frac{\epsilon^{-\alpha}}{D_f} \left(\int_0^y u_f dy + M_1 \right) \frac{\partial c_f^{(0)}}{\partial \xi}, \quad (\text{B } 1)$$

where the integration constant M_1 is determined by using the no-flux condition (2.20) and the velocity profile (2.7),

$$M_1 = - \int_0^1 u_f dy = - \left(\frac{\Psi}{6} + \frac{A}{2} + B \right), \quad (\text{B } 2)$$

and A and B are defined in (2.9). Integration of (B 1) yields

$$c_f^{(1)} = \frac{\epsilon^{-\alpha}}{D_f} \frac{\partial c_f^{(0)}}{\partial \xi} \left(M_2 + M_1 y + \int \int_0^y u_f d^2 y \right). \quad (\text{B } 3)$$

By postulating $\langle c_f^{(1)} \rangle = 0$ (Mikelic *et al.* 2006), we can solve for M_2 ,

$$M_2 = - \left(\frac{\Psi}{120} + \frac{A}{24} + \frac{B}{2} + \frac{M_1}{2} \right). \quad (\text{B } 4)$$

Inserting (B 4) and (B 2) in (B 3) leads to

$$c_f^{(1)} = M(y) \frac{\epsilon^{-\alpha}}{D_f} \frac{\partial c_f^{(0)}}{\partial \xi}, \quad (\text{B } 5)$$

where

$$M(y) = \frac{\Psi}{24} y^4 + \frac{A}{6} y^3 + \frac{B}{2} y^2 + M_1 y + M_2. \quad (\text{B } 6)$$

Similarly, double integration of (A 5b) yields a solution for $c_m^{(1)}$ in the following form:

$$c_m^{(1)} = \frac{\epsilon^{-\alpha}}{D_{my}} N(y) \frac{\partial c_m^{(0)}}{\partial \xi}, \quad (\text{B } 7)$$

where

$$N(y) = \frac{E}{\lambda^2} e^{\lambda y} + \frac{F}{\lambda^2} e^{-\lambda y} - \frac{\Psi}{2\lambda^2} y^2 - \left(\frac{E}{\lambda} - \frac{F}{\lambda} \right) y + N_1 y + N_2. \quad (\text{B } 8)$$

Here, E and F are defined in (2.9) and N_1 and N_2 are integration constants. The constant N_1 is determined by imposing the boundary condition (2.20),

$$N_1 = \frac{E}{\lambda} (1 - e^{-\lambda h}) - \frac{F}{\lambda} (1 - e^{-\lambda h}) + \frac{\Psi h}{\lambda^2}, \quad (\text{B } 9)$$

and N_2 is determined by imposing $\langle c_m^{(1)} \rangle = 0$,

$$N_2 = - \left[\frac{E}{h\lambda^3} (1 - e^{-\lambda h}) - \frac{F}{h\lambda^3} (1 - e^{\lambda h}) - \frac{\Psi}{6\lambda^2} h^2 + \frac{h}{2} \left(\frac{E}{\lambda} - \frac{F}{\lambda} \right) - \frac{N_1 h}{2} \right]. \quad (\text{B } 10)$$

Equations (B 7), (B 9) and (B 10) fully define $c_m^{(1)}$.

Appendix C. Order $O(\epsilon)$: $c_f^{(2)}$ and $c_m^{(2)}$ solutions

By inserting (B 5) into (A 4b), we obtain

$$\epsilon^{-\alpha} \frac{\partial c_f^{(0)}}{\partial t} + \frac{\epsilon^{-2\alpha}}{D_f} u_f M \frac{\partial^2 c_f^{(0)}}{\partial \xi^2} = D_f \frac{\partial^2 c_f^{(0)}}{\partial \xi^2} + D_f \frac{\partial^2 c_f^{(2)}}{\partial y^2}, \quad (\text{C } 1)$$

which provides an equation for $c_f^{(2)}$. Averaging (C 1) gives

$$\epsilon^{-\alpha} \frac{\partial c_f^{(0)}}{\partial t} + \frac{\epsilon^{-2\alpha}}{D_f} \langle u_f M \rangle \frac{\partial^2 c_f^{(0)}}{\partial \xi^2} = D_f \frac{\partial^2 c_f^{(0)}}{\partial \xi^2} - D_f \left[\frac{\partial c_f^{(2)}}{\partial y} \right]_{y=0}. \quad (\text{C } 2)$$

Subtracting (C 2) from (C 1) yields

$$\frac{\epsilon^{-2\alpha}}{D_f} (u_f M - \langle u_f M \rangle) \frac{\partial^2 c_f^{(0)}}{\partial \xi^2} = D_f \frac{\partial^2 c_f^{(2)}}{\partial y^2} + D_f \left[\frac{\partial c_f^{(2)}}{\partial y} \right]_{y=0}, \quad (\text{C } 3)$$

where the boundary term can be rewritten using (A 9). This leads to

$$\frac{\partial^2 c_f^{(2)}}{\partial y^2} = \frac{\epsilon^{-2\alpha}}{D_f^2} (u_f M - \langle u_f M \rangle) \frac{\partial^2 c_f^{(0)}}{\partial \xi^2} - \frac{\phi D_{my}}{D_f} \left[\frac{\partial c_m^{(2)}}{\partial y} \right]_{y=0}. \quad (\text{C } 4)$$

Integration in y gives

$$\frac{\partial c_f^{(2)}}{\partial y} = \frac{\epsilon^{-2\alpha}}{D_f^2} \frac{\partial^2 c_f^{(0)}}{\partial \xi^2} \int_0^y (u_f M - \langle u_f M \rangle) dy + \frac{\phi D_{my}}{D_f} \left[\frac{\partial c_m^{(2)}}{\partial y} \right]_{y=0} (K_1 - y), \quad (\text{C } 5)$$

where K_1 is an integration constant. Using the no-flux boundary condition at $y = 1$ (2.20), while observing that $\int_0^1 (u_f M - \langle u_f M \rangle) dy = \langle u_f M - \langle u_f M \rangle \rangle = 0$, yields

$$K_1 = 1. \quad (\text{C } 6)$$

Integrating (C 5) in y once more leads to

$$c_f^{(2)} = \frac{\epsilon^{-2\alpha}}{D_f^2} \frac{\partial^2 c_f^{(0)}}{\partial \xi^2} \iint_0^y (u_f M - \langle u_f M \rangle) d^2 y + \frac{\phi D_{my}}{D_f} \left[\frac{\partial c_m^{(2)}}{\partial y} \right]_{y=0} \left(K_2 + y - \frac{1}{2} y^2 \right). \quad (\text{C } 7)$$

Since $\langle c_f^{(2)} \rangle = 0$, then

$$\int_0^1 \left(K_2 + y - \frac{1}{2} y^2 \right) dy = 0 \quad \text{or} \quad K_2 = -\frac{1}{3}. \quad (\text{C } 8)$$

Finally,

$$c_f^{(2)} = \frac{\epsilon^{-2\alpha}}{D_f^2} \frac{\partial^2 c_f^{(0)}}{\partial \xi^2} \iint_0^y (u_f M - \langle u_f M \rangle) d^2 y + \frac{\phi D_{my}}{D_f} \left[\frac{\partial c_m^{(2)}}{\partial y} \right]_{y=0} \left(-\frac{1}{2} y^2 + y - \frac{1}{3} \right). \quad (\text{C } 9)$$

A similar procedure leads to

$$c_m^{(2)} = \frac{\epsilon^{-2\alpha}}{D_{my}^2} \frac{\partial^2 c_m^{(0)}}{\partial \xi^2} \iint_0^y (u_m N - \langle u_m N \rangle) d^2 y + \frac{D_f}{\phi D_{my}} \left[\frac{\partial c_f^{(2)}}{\partial y} \right]_{y=0} \left(-\frac{1}{2} y^2 - y h + \frac{1}{3} h^2 \right). \quad (\text{C } 10)$$

Appendix D. Upscaled equations

Applying the averaging operator to (A 1) and (A 2) while accounting for the third boundary condition (2.20) leads to

$$\begin{aligned} & \frac{\partial \langle c_f \rangle}{\partial t} + \epsilon^{-1/2} \langle u_f \rangle \frac{\partial c_f^{(0)}}{\partial \xi} + \left\langle u_f \frac{\partial c_f^{(1)}}{\partial \xi} \right\rangle + \epsilon^{-1/2} \left\langle u_f \frac{\partial c_f^{(2)}}{\partial \xi} \right\rangle \\ & = \epsilon^\alpha D_f \frac{\partial^2 \langle c_f \rangle}{\partial \xi^2} - \epsilon^{\alpha-1/2} D_f \left[\frac{\partial c_f^{(1)}}{\partial y} \right]_{y=0} - \epsilon^{\alpha-1} D_f \left[\frac{\partial c_f^{(2)}}{\partial y} \right]_{y=0} \end{aligned} \quad (\text{D } 1)$$

and

$$\begin{aligned} & \frac{\partial \langle c_m \rangle}{\partial t} + \epsilon^{-1/2} \langle u_m \rangle \frac{\partial c_m^{(0)}}{\partial \xi} + \left\langle u_m \frac{\partial c_m^{(1)}}{\partial \xi} \right\rangle + \epsilon^{1/2} \left\langle u_m \frac{\partial c_m^{(2)}}{\partial \xi} \right\rangle \\ & = \epsilon^\alpha D_{mx} \frac{\partial^2 \langle c_m \rangle}{\partial \xi^2} - \epsilon^{\alpha-1/2} \frac{D_{my}}{h} \left[\frac{\partial c_m^{(1)}}{\partial y} \right]_{y=0} - \epsilon^{\alpha-1} \frac{D_{my}}{h} \left[\frac{\partial c_m^{(2)}}{\partial y} \right]_{y=0} \end{aligned} \quad (\text{D } 2)$$

respectively, since $\langle c_j^{(1)} \rangle = \langle c_j^{(2)} \rangle = 0$ and $\langle c_j \rangle = \langle c_j^{(0)} \rangle$, with $j = \{f, m\}$. In order to close (D 1) and (D 2), the non-local advective terms and the boundary terms ought to be expressed in terms of macroscale quantities. Averaging (A 4c) leads to

$$\left\langle u_f \frac{\partial c_f^{(2)}}{\partial \xi} \right\rangle = 0, \quad (\text{D } 3)$$

since $\langle c_f^{(1)} \rangle = 0$. Inserting (B 5) in (D 1) while accounting for (D 3) gives

$$\begin{aligned} & \frac{\partial \langle c_f \rangle}{\partial t} + \epsilon^{-1/2} \langle u_f \rangle \frac{\partial c_f^{(0)}}{\partial \xi} + \epsilon^{-\alpha} \frac{\langle u_f M \rangle}{D_f} \frac{\partial^2 c_f^{(0)}}{\partial \xi^2} \\ & = \epsilon^\alpha D_f \frac{\partial^2 \langle c_f \rangle}{\partial \xi^2} - \epsilon^{\alpha-1/2} D_f \left[\frac{\partial c_f^{(1)}}{\partial y} \right]_{y=0} - \epsilon^{\alpha-1} D_f \left[\frac{\partial c_f^{(2)}}{\partial y} \right]_{y=0}. \end{aligned} \quad (\text{D } 4)$$

Similarly, for the matrix we obtain

$$\begin{aligned} & \frac{\partial \langle c_m \rangle}{\partial t} + \epsilon^{-1/2} \langle u_m \rangle \frac{\partial c_m^{(0)}}{\partial \xi} + \epsilon^{-\alpha} \frac{\langle u_m N \rangle}{D_{my}} \frac{\partial^2 c_m^{(0)}}{\partial \xi^2} \\ & = \epsilon^\alpha D_{mx} \frac{\partial^2 \langle c_m \rangle}{\partial \xi^2} - \epsilon^{\alpha-1/2} \frac{D_{my}}{h} \left[\frac{\partial c_m^{(1)}}{\partial y} \right]_{y=0} - \epsilon^{\alpha-1} \frac{D_{my}}{h} \left[\frac{\partial c_m^{(2)}}{\partial y} \right]_{y=0}. \end{aligned} \quad (\text{D } 5)$$

The last step to close (D 4) and (D 5) is to determine the boundary flux terms $[\partial_y c_f^{(1)}]_{y=0}$ and $[\partial_y c_f^{(2)}]_{y=0}$. Combining the boundary condition (A 8) with (B 7) gives

$$\frac{\partial c_m^{(1)}}{\partial y} = \epsilon^{-\alpha} \frac{N'}{D_{my}} \frac{\partial c_m^{(0)}}{\partial \xi}, \quad (\text{D } 6)$$

where $N' = dN/dy$ and $[N']_{y=0} = N_1$, see (B 8). Therefore,

$$\left[\frac{\partial c_m^{(1)}}{\partial y} \right]_{y=0} = \epsilon^{-\alpha} \frac{N_1}{D_{my}} \frac{\partial \langle c_m \rangle}{\partial \xi}. \quad (\text{D } 7)$$

Combining (D7) with (A8) gives

$$\left[\frac{\partial c_f^{(1)}}{\partial y} \right]_{y=0} = \epsilon^{-\alpha} \frac{\phi N_1}{D_f} \frac{\partial \langle c_m \rangle}{\partial \xi}. \quad (\text{D } 8)$$

Similarly, for the matrix,

$$\left[\frac{\partial c_m^{(1)}}{\partial y} \right]_{y=0} = \epsilon^{-\alpha} \frac{M_1}{\phi D_{my}} \frac{\partial \langle c_f \rangle}{\partial \xi}. \quad (\text{D } 9)$$

From (C9) we obtain

$$\left[\frac{\partial c_m^{(2)}}{\partial y} \right]_{y=0} = -\frac{3D_f}{\phi D_{my}} c_f^{(2)}(y=0). \quad (\text{D } 10)$$

At the interface $y=0$, continuity of concentration (A6) imposes

$$\epsilon c_m^{(2)} = c_f^{(0)} - c_m^{(0)} + O(\sqrt{\epsilon}) \quad \text{and} \quad \epsilon c_f^{(2)} = c_m^{(0)} - c_f^{(0)} + O(\sqrt{\epsilon}). \quad (\text{D } 11a,b)$$

Hence,

$$\left[\frac{\partial c_m^{(2)}}{\partial y} \right]_{y=0} = -\frac{3D_f}{\phi \epsilon D_{my}} (c_f^{(0)} - c_m^{(0)}) = -\frac{3D_f}{\phi \epsilon D_{my}} (\langle c_f \rangle - \langle c_m \rangle), \quad (\text{D } 12)$$

$$\left[\frac{\partial c_m^{(2)}}{\partial y} \right]_{y=0} = -\frac{3D_f}{\phi \epsilon D_{my}} (\langle c_f \rangle - \langle c_m \rangle). \quad (\text{D } 13)$$

A similar relation can be found for the channel,

$$\left[\frac{\partial c_f^{(2)}}{\partial y} \right]_{y=0} = \frac{3\phi D_{my}}{\epsilon h D_f} (\langle c_f \rangle - \langle c_m \rangle). \quad (\text{D } 14)$$

Inserting (D8), (D9), (D12) and (D14) into (D4) and (D5) gives

$$\begin{aligned} & \frac{\partial \langle c_f \rangle}{\partial t} + \frac{1}{\sqrt{\epsilon}} \langle u_f \rangle \frac{\partial \langle c_f \rangle}{\partial \xi} + \frac{\epsilon^{-\alpha}}{D_f} \langle u_f M \rangle \frac{\partial^2 \langle c_f \rangle}{\partial \xi^2} \\ & = \epsilon^\alpha D_f \frac{\partial^2 \langle c_f \rangle}{\partial \xi^2} - \epsilon^{\alpha-1} \sqrt{\epsilon} \phi \epsilon^{-\alpha} N_1 \frac{\partial \langle c_m \rangle}{\partial \xi} - \epsilon^{\alpha-1} \frac{3\phi D_{my}}{\epsilon h} (\langle c_f \rangle - \langle c_m \rangle) \end{aligned} \quad (\text{D } 15)$$

and

$$\begin{aligned} & \frac{\partial \langle c_m \rangle}{\partial t} + \frac{1}{\sqrt{\epsilon}} \langle u_m \rangle \frac{\partial \langle c_m \rangle}{\partial \xi} + \frac{\epsilon^{-\alpha}}{D_{my}} \langle u_m N \rangle \frac{\partial^2 \langle c_m \rangle}{\partial \xi^2} \\ & = \epsilon^\alpha D_{mx} \frac{\partial^2 \langle c_m \rangle}{\partial \xi^2} + \frac{M_1}{\phi h \sqrt{\epsilon}} \frac{\partial \langle c_f \rangle}{\partial \xi} + \epsilon^{\alpha-1} \frac{D_{my}}{h} \frac{3D_f}{\phi \epsilon D_{my}} (\langle c_f \rangle - \langle c_m \rangle). \end{aligned} \quad (\text{D } 16)$$

By rescaling the axis back to the physical coordinate x , multiplying both sides by $\epsilon^{1-\alpha}$ and using the Péclet number definition, we obtain the macroscopic equations (3.5a) and (3.5b).

REFERENCES

- AL-CHIDIAC, M., MIRBOD, P., ANDREOPOULOS, Y. & WEINBAUM, S. 2009 Dynamic compaction of soft compressible porous materials: experiments on air–solid phase interaction. *J. Porous Media* **12** (11), 1019–1035.
- ARIS, R. 1956 On the dispersion of a solute in a fluid flowing through a tube. *Proc. R. Soc. Lond.* **235** (1200), 67–77.
- BATTIATO, I. 2012 Self-similarity in coupled Brinkman/Navier–Stokes flows. *J. Fluid Mech.* **699**, 94–114.
- BATTIATO, I. 2014 Effective medium theory for drag-reducing micro-patterned surfaces in turbulent flows. *Eur. Phys. J. E* **37** (19).
- BATTIATO, I., BANDARU, P. & TARTAKOVSKY, D. M. 2010 Elastic response of carbon nanotube forests to aerodynamic stresses. *Phys. Rev. Lett.* **105**, 144504.
- BATTIATO, I. & RUBOL, S. 2014 Single-parameter model of vegetated aquatic flows. *Water Resour. Res.* **50** (8), 6358–6369.
- BATTIATO, I. & VOLLMER, J. 2012 Flow-induced shear instabilities of cohesive granulates. *Phys. Rev. E* **86**, 031301.
- BEAVERS, G. S. & JOSEPH, D. D. 1967 Boundary conditions at a naturally permeable wall. *J. Fluid Mech.* **30** (01), 197–207.
- BODIN, J., DELAY, F. & DE MARSILY, G. 2003 Solute transport in a single fracture with negligible matrix permeability. 1. Fundamental mechanisms. *Hydrogeol. J.* **11** (4), 418–433.
- BOSO, F. & BATTIATO, I. 2013 Homogenizability conditions of multicomponent reactive transport processes. *Adv. Water Resour.* **62**, 254–265.
- BOUQUET, L. & LAUGA, E. 2011 A smooth future? *Nat. Mater.* **10**, 334–337.
- BRENNER, H. 1987 *Transport Processes in Porous Media*. McGraw-Hill.
- CUI, J., DANIEL, D., GRINTHAL, A., LIN, K. & AIZENBERG, J. 2015 Dynamic polymer systems with self-regulated secretion for the control of surface properties and material healing. *Nat. Mater.* **14** (8), 790–795.
- DAVIS, A. M. J. & LAUGA, E. 2010 Hydrodynamic friction of fakir-like superhydrophobic surfaces. *J. Fluid Mech.* **661**, 402–411.
- DECK, C. P., NI, C., VECCHIO, K. S. & BANDARU, P. R. 2009 The response of carbon nanotube ensembles to fluid flow: applications to mechanical property measurement and diagnostics. *J. Appl. Phys.* **106** (7), 74304.
- DEJAM, M., HASSANZADEH, H. & CHEN, Z. 2014 Shear dispersion in a fracture with porous walls. *Adv. Water Resour.* **74**, 14–25.
- GHISALBERTI, M. 2009 Obstructed shear flows: similarities across systems and scales. *J. Fluid Mech.* **641**, 51–61.
- GILROY, S. & JONES, D. L. 2000 Through form to function: root hair development and nutrient uptake. *Trends Plant Sci.* **5**, 56–60.
- GOHARZADEH, A., KHALILI, A. & JØRGENSEN, B. B. 2005 Transition layer thickness at a fluid–porous interface. *Phys. Fluids* **17** (5), 057102.
- GRAY, W. G. & MILLER, C. T. 2005 Thermodynamically constrained averaging theory approach for modeling flow and transport phenomena in porous medium systems: 1. Motivation and overview. *Adv. Water Resour.* **28** (2), 161–180.
- GRIFFITHS, I. M., HOWELL, P. D. & SHIPLEY, R. J. 2013 Control and optimization of solute transport in a thin porous tube. *Phys. Fluids* **25** (3), 033101.
- GRUENBERGER, A., PROBST, C., HEYER, A., WIECHERT, W., FRUNZKE, J. & KOHLHEYER, D. 2013 Microfluidic picoliter bioreactor for microbial single-cell analysis: fabrication, system setup, and operation. *J. Vis. Exp.* (82), e50560.
- HORNE, R. N. & RODRIGUEZ, F. 1983 Dispersion in tracer flow in fractured geothermal systems. *Geophys. Res. Lett.* **10** (4), 289–292.
- HORNUNG, U. 1997 *Homogenization and Porous Media*. Springer.
- HOU, X., HU, Y., GRINTHAL, A., KHAN, M. & AIZENBERG, J. 2015 Liquid-based gating mechanism with tunable multiphase selectivity and antifouling behaviour. *Nature* **519**, 70–73.

- KAZEZYILMAZ-ALHAN, C. M. 2008 Analytical solutions for contaminant transport in streams. *J. Hydrol.* **348** (3), 524–534.
- LAUGA, E. & STONE, H. A. 2003 Effective slip in pressure-driven Stokes flow. *J. Fluid Mech.* **489**, 55–77.
- LE BARS, M. & WORSTER, M. G. 2006 Interfacial conditions between a pure fluid and a porous medium: implications for binary alloy solidification. *J. Fluid Mech.* **550**, 149–173.
- LI, X. M., REINHOUDT, D. & CREGO-CALAMA, M. 2007 What do we need for a superhydrophobic surface? A review on the recent progress in the preparation of superhydrophobic surfaces. *Chem. Soc. Rev.* **36**, 1350–1368.
- LIU, C., SHANG, J., KERISIT, S., ZACHARA, J. M. & ZHU, W. 2013 Scale-dependent rates of uranyl surface complexation reaction in sediments. *Geochim. Cosmochim. Acta* **105**, 326–341.
- LLOYD, F. E. 1942 *The Carnivorous Plants*. Read Books Ltd.
- MARMUR, A. 2004 The lotus effect: superhydrophobicity and metastability. *Langmuir* **20**, 3517–3519.
- MARSCHNER, H. & DELL, B. 1994 Nutrient uptake in mycorrhizal symbiosis. *Plant Soil* **159** (1), 89–102.
- MARUF, S. H., RICKMAN, M., WANG, L. IV, MERSCH, J., GREENBERG, A. R., PELLEGRINO, J. & DING, Y. 2013a Influence of sub-micron surface patterns on the deposition of model proteins during active filtration. *J. Membr. Sci.* **444**, 420–428.
- MARUF, S. H., WANG, L., GREENBERG, A. R., PELLEGRINO, J. & DING, Y. 2013b Use of nanoimprinted surface patterns to mitigate colloidal deposition on ultrafiltration membranes. *J. Membr. Sci.* **428**, 598–607.
- MIKELIC, A., DEVIGNE, V. & DUIJN, C. J. VAN 2006 Rigorous upscaling of the reactive flow through a pore, under dominant Peclet and Damkohler numbers. *SIAM J. Math. Anal.* **38** (4), 1262–1287.
- NEPF, H., GHISALBERTI, M., WHITE, B. & MURPHY, E. 2007 Retention time and dispersion associated with submerged aquatic canopies. *Water Resour. Res.* **43** (4), W04422.
- NEPF, H. M. 2012 Flow and transport in regions with aquatic vegetation. *Annu. Rev. Fluid Mech.* **44** (1), 123–142.
- NIKORA, V., GORING, D., MCEWAN, I. & GRIFFITHS, G. 2001 Spatially averaged open-channel flow over rough bed. *J. Hydraul. Engng.*
- OGATA, A. & BANKS, R. B. 1961 A solution of the differential equation of longitudinal dispersion in porous media. *US Geol. Surv. Prof. Pap.* **411-A**.
- OU, J., PEROT, B. & ROTHSTEIN, J. P. 2004 Laminar drag reduction in microchannels using ultrahydrophobic surfaces. *Phys. Fluids* **16** (12), 4635–4643.
- PAPKE, A. & BATTIATO, I. 2013 A reduced complexity model for dynamic similarity in obstructed shear flows. *Geophys. Res. Lett.* **40**, 1–5.
- REICHERT, P. & WANNER, O. 1991 Enhanced one-dimensional modeling of transport in rivers. *J. Hydraul. Engng* **117** (9), 1165–1183.
- ROTHSTEIN, J. P. 2010 Slip on superhydrophobic surfaces. *Annu. Rev. Fluid Mech.* **42**, 89–109.
- ROUBINET, D., DREUZY, J.-R. & TARTAKOVSKY, D. M. 2012 Semi-analytical solutions for solute transport and exchange in fractured porous media. *Water Resour. Res.* **48** (1), W01542.
- SCHOLZ, I., BÜCKINS, M., DOLGE, L., ERLINGHAGEN, T., WETH, A., HISCHE, F., MAYER, J., HOFFMANN, S., RIEDERER, M. & RIEDEL, M. 2010 Slippery surfaces of pitcher plants: nepenthes wax crystals minimize insect attachment via microscopic surface roughness. *J. Expl Biol.* **213**, 1115–1125.
- STROOCK, A. D., DERTINGER, S. K. W., AJDARI, A., MEZIC, I., STONE, H. A. & WHITESIDES, G. M. 2002 Chaotic mixer for microchannels. *Science* **295**, 647–651.
- STROOCK, A. D. & WHITESIDES, G. M. 2003 Controlling flows in microchannels with patterned surface charge and topography. *Acc. Chem. Res.* **36**, 597–604.
- SUDICKY, E. A. & FRIND, E. O. 1982 Contaminant transport in fractured porous media: analytical solutions for a system of parallel fractures. *Water Resour. Res.* **18** (6), 1634–1642.
- TANG, D. H., FRIND, E. O. & SUDICKY, E. A. 1981 Contaminant transport in fractured porous media: analytical solution for a single fracture. *Water Resour. Res.* **17** (3), 555–564.

- TAYLOR, G. 1953 Dispersion of soluble matter in solvent flowing slowly through a tube. *Proc. R. Soc. Lond.* **219**, 186–203.
- VALDES-PARADA, F. J., OCHOA-TAPIA, J. A. & ALVAREZ-RAMIREZ, J. 2009 Validity of the permeability Carman–Kozeny equation: a volume averaging approach. *Physica A* **388** (6), 789–798.
- WEINBAUM, S., ZHANG, X., HAN, Y., VINK, H. & COWIN, S. C. 2003 Mechanotransduction and flow across the endothelial glycocalyx. *Proc. Natl Acad. Sci.* **100** (13), 7988–7995.
- WEINMAN, S. T. & HUSSON, S. M. 2016 Influence of chemical coating combined with nanopatterning on alginate fouling during nanofiltration. *J. Membr. Sci.* **513**, 146–154.
- WHITAKER, S. 1999 *The Method of Volume Averaging*. Kluwer.
- WU, Y.-S., YE, M. & SUDICKY, E. A. 2010 Fracture-flow-enhanced matrix diffusion in solute transport through fractured porous media. *Trans. Porous Med.* **81** (1), 21–34.
- YBERT, C., BARENTIN, C., COTTIN-BIZONNE, C., JOSEPH, P. & BOCQUET, L. 2007 Achieving large slip with superhydrophobic surfaces: scaling laws for generic geometries. *Phys. Fluids* **19**, 123601.